BUBBLY FLOW EXPERIMENT IN CHANNEL USING AN OPTICAL PROBE AND TRACKING ALGORITHM

A Thesis

by

ABDUL R. KHAN

Submitted to the Office of Graduate Studies of
Texas A&M University
in partial fulfillment of the requirements for the degree of

MASTER OF SCIENCE

August 2012

Major Subject: Nuclear Engineering

Bubbly Flow Experiment in Channel Using an Optical Probe and Tracking Algorithm

BUBBLY FLOW EXPERIMENT IN CHANNEL USING AN OPTICAL PROBE AND TRACKING ALGORITHM

A Thesis

by

ABDUL R. KHAN

Submitted to the Office of Graduate Studies of
Texas A&M University
in partial fulfillment of the requirements for the degree of

MASTER OF SCIENCE

Approved by:

Chair of Committee,	Yassin A. Hassan
Committee Members,	William H. Marlow
	Kalyan Annamalai
Head of Department,	Yassin A. Hassan

August 2012

Major Subject: Nuclear Engineering

ABSTRACT

Bubbly Flow Experiment in Channel Using an

Optical Probe and Tracking Algorithm. (August 2012)

Abdul R. Khan, B.S., New Jersey Institute of Technology

Chair of Advisory Committee: Dr. Yassin A. Hassan

In this study, the phenomenon of two-phase flow was investigated in a square channel. The experiment was performed with stagnant liquid conditions. The gas and liquid dynamics of the bubbly flow were observed in two regions far from the inlet. Air was inserted through a porous media at three superficial gas velocities: 4.6 mm/s, 2.5 mm/s, and 1.4 mm/s.

Two techniques were applied in the experiment to measure the bubbly flow: an optical probe and an in-house developed tracking algorithm. Measurements of the bubble interface velocity, void fraction, bubble frequency, time of flight, and Sauter mean diameter were obtained by using the optical probe. The duration of the probe measurements for all three flow rates and both regions lasted approximately 33 hours. The tracking algorithm was used to analyze the experimental data for two visual methods: shadowgraphy and Particle Tracking Velocimetry (PTV). Shadowgraphy provided gas-phase measurements of the bubble centroid velocity and its fluctuations, void fraction, bubble size, and Reynolds stresses. Five data sets were acquired for each flow rate, resulting in a total of 327,540 shadowgraphy images. Liquid parameters such

as the velocity, fluctuations in the velocity, and the Reynolds stresses were provided by PTV. Only one data set containing 10,918 images was obtained from liquid measurements for each flow rate. One data set was sufficient to provide reliable statistics since tracking two consecutive images lead to approximately 15,000 velocity vectors. The data obtained from this study was an effort to assist in the verification, validation, and improvement of two-phase flow simulations.

DEDICATION

For my family

TABLE OF CONTENTS

Page

Page

LIST OF FIGURES

Page

CHAPTER I

INTRODUCTION

1.1 Objective

The goal of this study was to measure two-phase flow parameters of bubbly flow in a square channel using Particle Tracking Velocimetry (PTV), shadowgraphy, and an optical probe. The experiment was performed using air and water as the working fluids. The gas was inserted at different flow rates. PTV was applied to obtain the liquid parameters caused by the gas traversing through the channel. Shadowgraphy and the optical probe were used to obtain parameters such as the void fraction distribution across the channel and bubble velocity, frequency, and size. By performing this study, we hoped to supplement current computational codes and provide data that may assist in validating the codes.

1.2 Literature review

Although two-phase flow has been extensively studied and its applications vary in the industry, expanding knowledge of this phenomenon from experiments is vital for current simulations. Two-phase flows are employed due to their effective heat transfer rate. A particularly important application of two phase flow in the nuclear industry relates to safety systems. Some nuclear reactor safety systems release steam into a pool,

---

This thesis follows the style of International Journal of Multiphase Flow.

thereby creating bubbly flow. If designed and implemented incorrectly, the flow may cause damage to the surrounding structural materials. As a result, the overall safety of the reactor may be hindered. Moreover, there is a lack of experimental data to assist in improving current computational fluid dynamics (CFD) codes (Khan et al., 2011). Due to dissimilarity between experimental and simulated results, the data is required to supplement simulations and can be used to improve and validate codes. Also, more insight can be gained regarding two-phase flow by conducting various types of experiments and studies.

Multiple experimental efforts have been performed to obtain a better understanding of the parameters involved in two-phase flow by using different methods and techniques. Most of the important turbulence parameters have been measured using point intrusive methods. Normally, such instruments can achieve a temporal resolution necessary for the time scales required in many engineering systems. Based on probe point measurements from past experiments, models were created to compute two-phase flows (Roy et al., 2002; Yeoh et al., 2002, Končar et al., 2004, Ramstorfer et al., 2008).

Many studies in the past have implemented a probe to obtain two-phase flow information, but only a few will be mentioned. Revankar and Ishii (1992) presented the radial profiles of the void fraction, bubble velocity, bubble chord length, and interfacial area concentration at various gas flow rates using a double sensor probe. Experiments were performed inside a 5.08 cm inner diameter pipe and the superficial gas velocity ranged from 0.0034 – 0.1212 m/s with no liquid flow. The void fraction, interfacial area concentration, and Sauter mean diameter were compared with photographic

measurements analyzed by tracing the bubble projections on a paper and were found to be in good agreement. They did not have the capability to apply advanced visualization techniques currently available. Kiambi et al. (2003) compared bubble parameters measured from a double optical probe and imaging in a tank with a 15 cm square cross-section. The gas velocity was kept at a low rate for the capillary tubes of diameters 0.33 mm and 1.00 mm to produce bubble sizes of 2.15 mm and 4.50 mm, respectively. Multiple virtual probes were configured and introduced into the path of the bubbles reconstructed from the images, although it was unclear exactly how the virtual probe technique was performed. Their results showed that the probe underestimated the void fraction and overestimated the interfacial velocity. No liquid measurements were undertaken in their experiment.

The same methods, namely optical probe and imaging, were implemented by Chaumat et al. (2005) in a study measuring two-phase flow inside a 25 cm square cross-section tank. The gas flow rate varied between 0.8 – 4.0 mL/s. Their results showed that as the bubbles became larger (as flow rate increased) the deviation in the results between the probe and visualization increased. The liquid phase was not measured in their experiment.

Some experiments not mentioned above have also employed a dual-tip optical probe manufactured by RBI (France), such as the one used in this experiment, to measure two-phase flow parameters (Rensen and Roig, 2001; Chaumat et al., 2007; Lima Neto et al., 2008; Johansen, 2010).

Although intrusive methods and techniques have delivered valuable information, the lack of spatial resolution resulting from point measurements has limited the understanding of two-phase flows. Therefore, many visual measurement techniques have been implemented to improve the data. Due to the increase in spatial resolution, the techniques have helped obtain qualitative information. Thanks to the development of high speed camera electronics, visualization techniques have evolved into powerful tools capable of delivering whole-field quantitative information with temporal resolutions comparable to that of point measurement techniques (Khan et al., 2011). Examples of such non-intrusive techniques include Particle Image Velocimetry (PIV), Particle Tracking Velocimetry (PTV), Laser Doppler Velocimetry (LDV), and Magnetic Resonance Velocimetry (MRV). Laser Induced Fluorescence (LIF) is another flow visualization technique which has been applied along with PIV to measure two-phase flows (Sathe et al., 2010; Dahikar et al., 2010). Since the point measurement instruments are spatially limited, they are unable to provide whole-field (2-D) data and may not be used as frequently as PIV and other such methods.

Shadowgraphy is a specific PTV method that does not employ particle seeding with a laser as its illumination source. Usually, halogen lamps or LEDs (Light Emitting Diodes) are the light source for illumination. This method does not require costly or high-powered lasers and is a simple method to obtain bubble dynamics. It is a non-intrusive method and provides a 2-D velocity field. Bubble velocity, size, and void fraction can be obtained with this method, although an efficient algorithm should be implemented.

Lindken and Merzkirch (2002) performed an experiment in which they applied similar 2-D measurement techniques used in the present study: PIV and shadowgraphy. They injected bubbles at a Reynolds number of 1,400 into a square tank filled with stagnant liquid and measured the bubble and liquid velocity with a camera. Even though they were able to measure the velocity of the two phases simultaneously, their results did not include information such as the distributions of void fraction and bubble size. Zaruba et al. (2005) measured the velocity and size of bubbles in a rectangular bubble column 10 cm in width and 2 cm in depth. The bubbles were inserted through an aquarium porous stone with a range of superficial gas velocities of 1-6 mm/s. The only method utilized was similar to shadowgraphy. The velocity was calculated by tracking the center of mass of the bubble. To measure the size of the bubble, a method was proposed in which only spherical and elliptical bubbles were considered. Due to its limitation, they concluded that the method would have to be improved. Their results did not include any information pertaining to the liquid velocity.

CHAPTER II

BUBBLY FLOW STUDY IN SQARE CHANNEL

2.1 Experiment description

The experiment was conducted inside a large glass tank (Fig. 1) with inner dimensions of 91.44 cm in length, 30.48 cm in width, and 63.50 cm in height. The tank walls had a thickness of 1.27 cm. The Starphire glass used to construct the tank allows high transmission of visible light. It also had a low iron composition and provides a clearer view as compared to regular glass (Fig. 2). The tank was left rimless; the top was kept open to allow accessibility to instrumentation and other necessary materials located inside the tank (fittings, channel, etc.). Two holes with a diameter of 2.54 cm were made on the bottom plate. The hole in the middle of the tank was made to drain the liquid inside. The second hole was also in the middle but was made 3.81 cm away from of one of the walls. It allowed the air to pass through the bottom plate and enter the tank. The hole was designed close to the wall for imaging purposes. If it was made further away from the wall, the clarity of the flow would decrease and the camera lens would have to change to visualize the flow.

The water was supplied from a nearby line at room temperature (20-22 °C). A bulkhead fitting was placed in each hole to prevent the water from leaking. The fitting allowed for air to enter the tank when taking measurements and water to exit the tank when draining. The tank was filled with 48.26 cm of water and all measurements were taken with stagnant water conditions. A porous tube was inserted into a Swagelok fitting,

Figure 1: Glass tank used in this experiment.

Figure 2: Image of regular glass on the left and Starphire glass on the right (courtesy of Glasscages.com).

which was placed into the bulkhead fitting. The tube itself consisted of a 0.95 cm heavy glass walled side, which was compress-fitted into the Swagelok. It opened to a 2.15 cm (inner diameter) porous disk on the other side. For air to enter the tank, it passed through small pores located randomly throughout the disk in the porous tube. The pores on the disk ranged from 40-60 μm. The combined Swagelok and porous tube fitting (Fig. 3) extended 6.70 cm from the inside of the tank.

The square channel used to observe bubbly flow was placed over the porous tube in the tank. The height of water in the channel and the tank was the same. The extruded acrylic channel had a wall thickness of 0.16 cm, length (and width) of 2.2 cm, and a height of 61.0 cm. A slot of width 0.48 cm and length 3.81 cm was milled through one of the sides at a height of 40.64 cm for the optical probe to enter the channel horizontally. Another slot 3.81 cm below this region was milled with the same width but a length of 2.54 cm. Since the slots were larger than the area required for probe entrance, excess room above and below the probe was covered when the probe was positioned in the slot. The complete channel and a milled test portion can be seen in Fig. 4.

The air introduced into the tank was also taken from a nearby line at room temperature. The air inlet pressure was kept constant at 35 psig by a pressure regulator. A high efficiency particulate air (HEPA) filter was placed in the path of the air-flow to prevent any debris from damaging the flow meter and enter the tank. The control valve was placed before the HEPA filter and the flow meter in order to regulate the desired flow rate for the experiment. Three superficial gas velocities (j_g) were applied to produce

Figure 3: Images showing porous tube compress fitted into the Swagelok (A) and pores in porous disk (B).

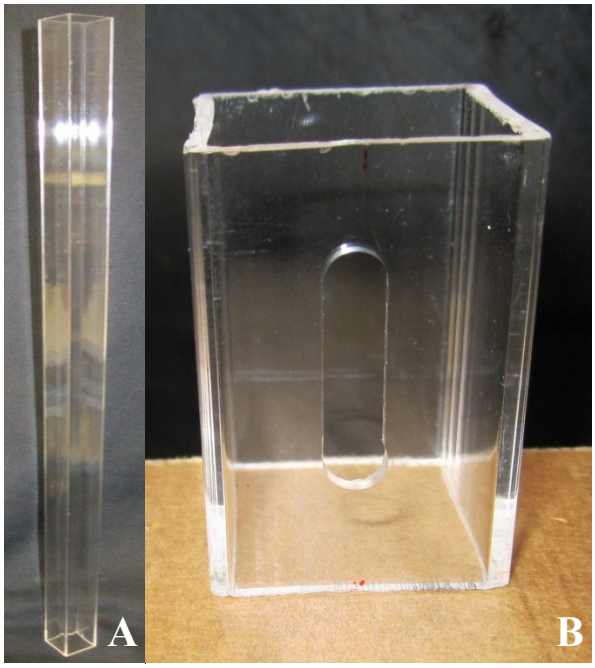

Figure 4: Images of the acrylic channel (A) and a milled test portion (B). Note: images are not to scale.

the bubbly flow: 4.6 mm/s, 2.5 mm/s, and 1.4 mm/s. The superficial gas velocity is defined as

$$j_g = \frac{Q_g}{A} \tag{1}$$

where Q_g is the gas volumetric flow rate and A is the flow area before entering the porous media. The flow rates were chosen to study a range of different bubble sizes and velocities. A flow meter, ranging from 0-100 mL/min, placed in the flow path allowed viewing and setting the flow rates. The flow meter was more accurate than a variable flow meter used in previous experiments. Any fluctuations in the flow rate were shown immediately, while the flow rates displayed by the variable flow meter were unreliable.

The Photron camera (Fig. 5) in the experiment was synchronized with the laser to record images of the liquid phase with 30 μm fluorescent tracer particles (Fig. 6). The particles would only fluoresce when illuminated with a certain wavelength of light; in this case, green light (532 nm). The laser system consisted of a diode pumped Nd:YAG laser head system operating at 80 mJ/pulse. A chilling unit provided water to cool the laser.

The camera provided higher resolution (1024 pixels x 1024 pixels) than other available cameras (800 pixels x 600 pixels). It was installed on translational stages that were controlled via a computer, making it convenient to switch between the two regions. In each region, measurements were taken with PTV, shadowgraphy, and the optical probe. PTV measurements were not performed simultaneously with shadowgraphy and the optical probe for different reasons. First, different channels were used for studying each phase in the bubbly flow. Slots on the side of the channel in probe-shadowgraphy

Figure 5: Photron camera used in the experiment shown with alternate lens.

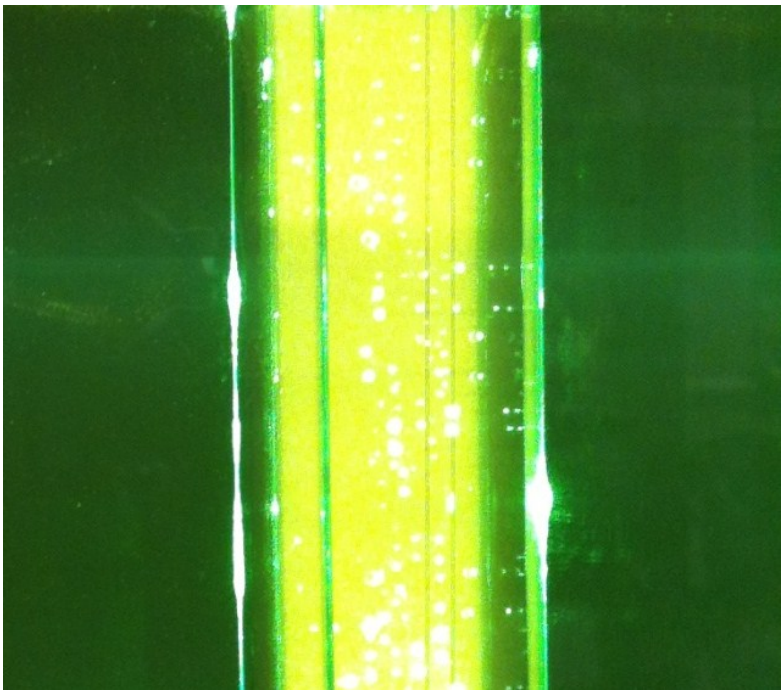

Figure 6: Laser light illuminating the fluorescent particles (yellow plane) and bubbles (white circles) from both sides.

measurements allowed movement of the probe into the channel. If the same channel had been used for PTV, most of the particles would leak through the slots into the tank, and this was highly undesired. Second, illumination would be a problem if the particles were prevented from leaking into the tank by covering the slots. In that case the channel would not be illuminated from both sides; the covered side would block the laser light from entering the channel. Finally, all three methods performed measurements on different time scales. The optical probe measurements lasted a little over 5 hours, shadowgraphy measurements took approximately 2.5 hours, and PTV measurements concluded after 12-13 minutes.

The experiment focused on two different regions far from the inlet where high-zoom studies involving liquid and bubble dynamics were performed (Fig. 7). The regions coincided with the location of the slots milled for the probe entrance. From henceforth, these two regions will be referred to as region 1 (slot 2.54 cm in length) and region 2 (slot 3.81 cm in length). Although measurements in each region were performed separately, it was desired to have measurements from the optical probe and shadowgraphy start at the same time as these two methods focused on obtaining the same parameters, namely bubble dynamics. Therefore the two methods observed the same region. It should be noted that if shadowgraphy and the optical probe are in the same region, the probe will cause disturbance to the flow and shadowgraphy will not deliver correct measurements. To prevent this, the area viewed by shadowgraphy was slightly below the position of the optical probe. This ensured that the bubble-probe interactions would occur above the shadowgraphy region and cause no erroneous

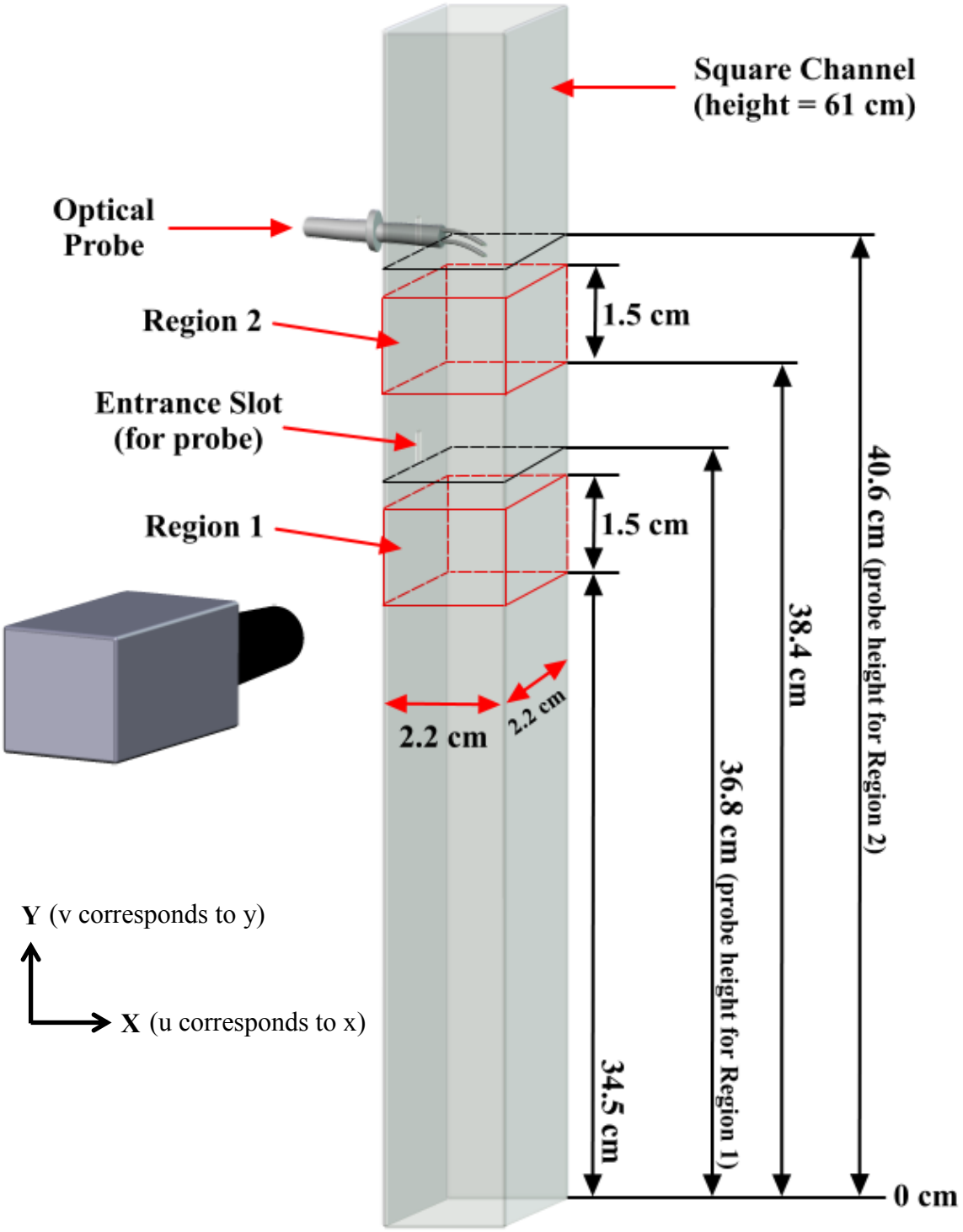

Figure 7: Schematic of channel with heights and dimensions of the regions observed.

measurements in shadowgraphy analysis. Another disturbance occurs from the milled slot on the left side of the channel. The results from previous test experiments showed a skewed distribution resulting from the slot. To avoid the issue, the optical probe and shadowgraphy techniques were applied to the right half of the channel and the other half was assumed to be symmetric. For region 1 the visual methods covered an area of 2.2 cm x 1.5 cm starting at 34.5 cm and the probe was placed at a height of 36.8 cm. The same sized region was covered for region 2 starting at 38.4 cm, but the probe measurements were performed at a height of 40.6 cm.

2.2 Applied methods

In this section, the methods and their application for measurements are briefly described. The optical probe was only capable of providing gas phase parameters. Data pertaining to both phases was obtained with shadowgraphy and PTV. It should be mentioned that the same tracking algorithm was applied when mentioning shadowgraphy and PTV. The seeding (tracer particles) and the illumination are the main differences between the two methods.

2.2.1 Optical probe

The dual-tip optical probe was able to provide average gas phase parameters such as the void fraction, bubble frequency (average number of bubbles per minute at each position), time of flight of the bubbles, bubble interface velocity, and the Sauter mean diameter. The probe had a different measurement technique compared to shadowgraphy

and PTV methods. It provided point measurements in 16 different radial positions in each region at different times. No cameras or illumination sources were required for this technique. The measurement system supplied by RBI Instruments consisted of the optical probe, a signal processing optoelectronic unit, and an interface board needed to establish communication between the computer and optoelectronic unit.

The probe takes advantage of the physics between two mediums, air and water (Fig. 8). The optical fiber, manufactured from glass, relays the signal in the probe. Internal reflection allows the propagation of light when transmitting or receiving signals. The light source is located in the optoelectronic unit. When the probe tip senses a bubble (a different medium) some of the light reflects back through the fiber because glass has a higher index of refraction than air. There was no reflection of light in water since the calibration was performed in the gas (air) with a threshold level. The optoelectronic unit creates a signal produced by the reflected light from the probe-bubble interaction. The detection of the bubble occurs only if the signal is greater than or equal to the threshold level. This signal has a rising edge when the tip enters the bubble and a falling edge when it leaves the bubble and enters the water. Based on the amount of time each tip remains inside the bubble and knowledge of other calculated parameters, the chord length and Sauter mean diameter can be obtained. The signal also assists in obtaining the void fraction (Vejražka et al., 2010).

Even though optical probes have spatial limitations, they are effective tools to obtain bubble properties. There are times when some visual techniques cannot be implemented for measurements. For example, if the experiment is performed in an

apparatus made of non-transparent material or a large void fraction exists, imaging techniques cannot be applied (Chaumat et al., 2005). In that case, an optical probe would be beneficial. An automatic measurement system assisted in performing probe measurements. The system consisted of a translational stage on which the probe was placed, allowing for horizontal movement in the channel. Once the probe was positioned in the center of the channel, the translational stage and the probe software were initiated. The probe acquired 20 minutes of data by obtaining ten 2-mintue measurements in each location. Once the measurements concluded, the probe automatically moved to the next location and started measurements. This continued until data was taken in all 16 positions for each flow rate. After completing the measurements for one flow rate, the

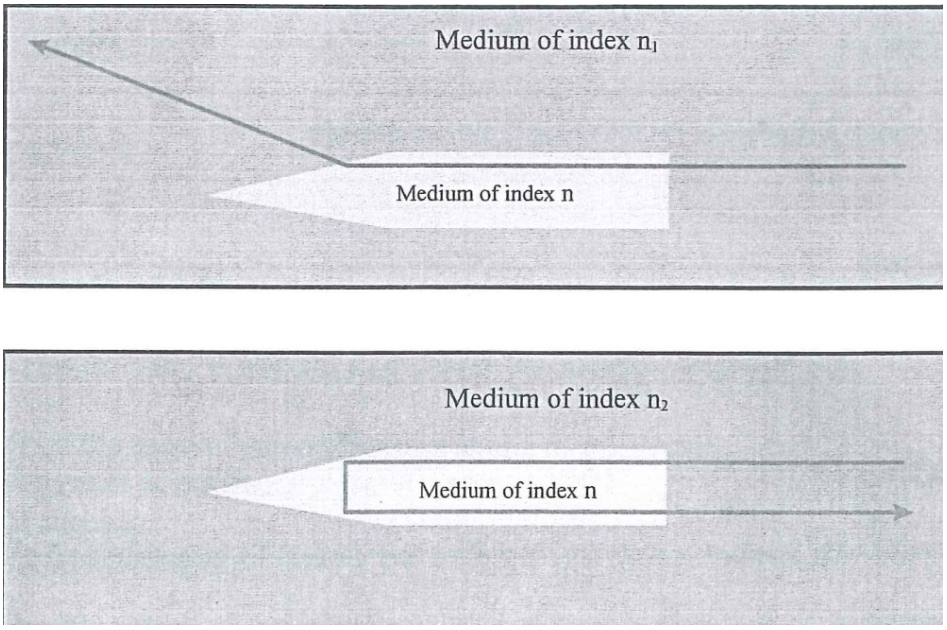

Figure 8: Images showing the light path when the tip is in water (top) and when a bubble is detected (bottom).

probe was moved back to the original position (center of channel) and the same process began for the next flow rate. The probe was moved vertically to region 2 when data was acquired all three flow rates in region 1. The above procedure repeated for each flow rate in the second region.

It will be worthwhile to describe the calculation of the parameters obtained from the optical probe, as described in the optical probe software manual. All calculations are performed internally by the software. The user has to enter one main parameter before starting the measurements: the distance between the two probe tips. A distance of 1.4 mm was entered into the software. Once the data was acquired, the software would perform the calculations based on the different values measured. The void fraction (α) was calculated as

$$\alpha = \frac{T_{gas}}{T_{acq}} \tag{2}$$

where T_{gas} was the amount of time spent inside a bubble by the probe tip and T_{acq} was the total acquisition time of one measurement, in this case being two minutes. The probe did not provide the conventional void fraction consisting of the area occupied by the gas and the total area. It is a point measurement technique and calculated parameters based on time.

The bubble number (N_b) was essentially the number of bubbles (signals) detected by the probe for each radial position, and N_b divided by T_{acq} provided the bubble frequency, f_b. The time it took for the bubble to travel from one tip to the other was called the time of flight (T_{flight}), which was necessary in calculating the bubble interface

velocity:

$$v_b = \frac{d}{T_{flight}} \tag{3}$$

where d was the distance between the probe tips. The time of flight was the only variable that affected the bubble velocity since d was fixed and could not be changed during the measurements. The Sauter mean diameter was calculated as

$$d_{32} = \frac{3 v_b \alpha}{2 f_b} \tag{4}$$

Although the Sauter mean diameter (also referred to as d_{SMD}) is defined as the ratio of the volume of a particle to its surface area, equation (4) was a simplified relation (Kataoka et al., 1986; Chaumat et al., 2005) due to the point measurement nature of the probe.

2.2.2 PTV and shadowgraphy

The tracking algorithm served as the primary method for measuring and obtaining 2-D parameters from the visual methods of both phases. The in-house developed algorithm, originally developed by Canaan et al. (1992), has been improved since it was developed and is capable of detecting and estimating the centroid of the particles. Afterwards, it performs tracking between consecutive images by matching the particles through a cross-correlation method. For a more detailed description see Estrada-Perez (2004) and Estrada-Perez and Hassan (2010).

The tracking algorithm analyzed data obtained from the liquid phase through PTV. It provided average liquid phase parameters: axial and radial components of the

velocity, fluctuations in the liquid velocity (calculated from the root mean square; RMS), and the Reynolds stresses. In order to track the liquid, fluorescent particles were inserted from the top of the channel. Laser light sheets were incident from both sides of the channel (Figs. 9 and 10). This was very beneficial for studying the flow in the channel. Dual illumination provided quality images in which all areas in the region were illuminated. It also made tracking of the liquid possible on both sides of the bubble. When a bubble is illuminated from one side, the particles on the other side receive little or no illumination at all and the particles will not be tracked in that area of the channel. After inserting the particles, time was given for the particles to spread throughout the channel before the gas was inserted. Air was inserted when the particles were uniformly distributed. Measurements were taken some time after bubble formation to allow the flow to develop and to reach the desired flow rate. Next, the camera was signaled to record the flow. The signal supplied to the camera was synchronized to the initial pulse from the laser. Although the laser operated at 30 Hz, the time in between the two laser pulses (one from each lamp) was set to 0.001 seconds corresponding to 1000 frames per second (fps). Two consecutive signals sent to the camera had an interval of five pulses in between. Since the camera was capable of recoding the images when triggered with the incoming signal, this ensured that there would be a new set of bubbles in consecutive image pairs i.e. two images would be captured at 1000 fps, a five pulse-time interval wait would occur, and the next two images would be captured at 1000 fps. This process continued until all images had been captured. As will be shown later on, this method had a significant effect on the results. After all data was obtained it was stored on an external

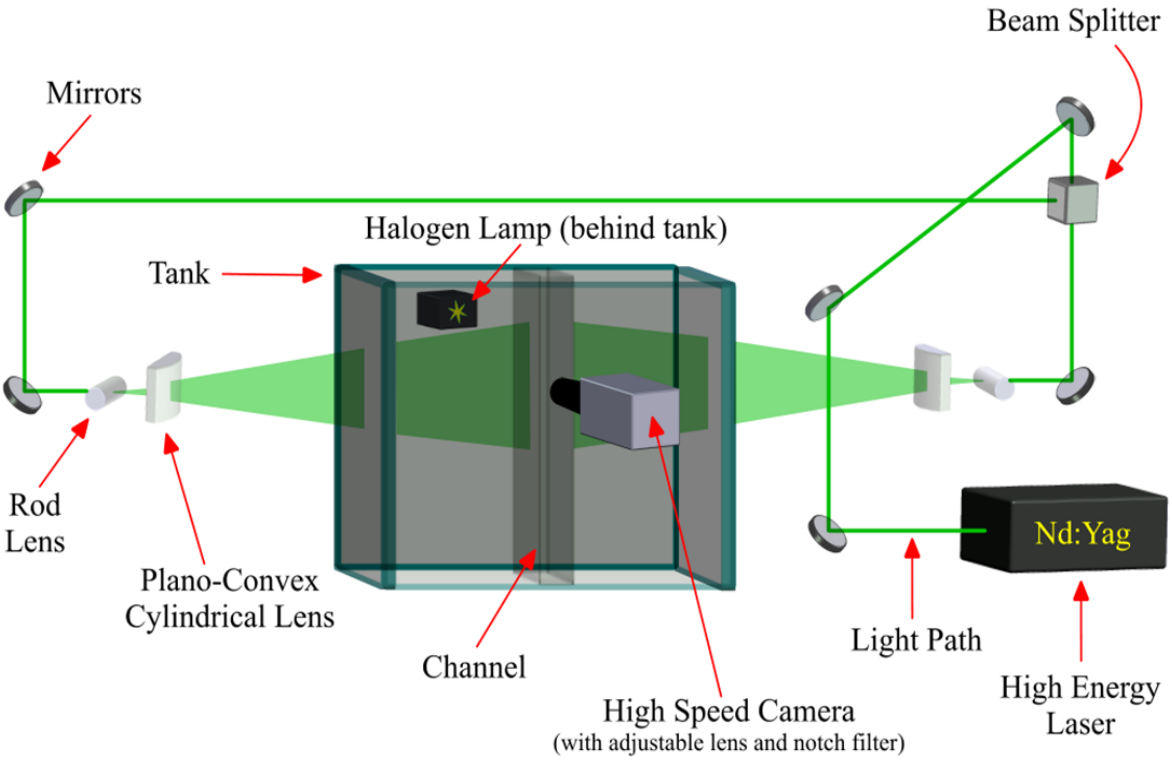

Figure 9: Schematic of experiment with dual illumination.

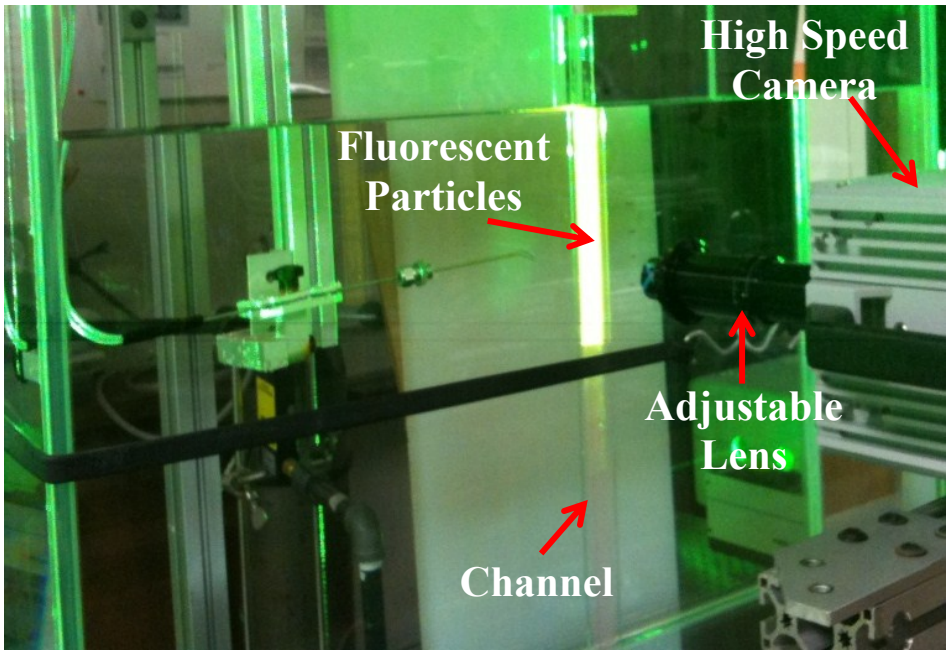

Figure 10: Image showing fluorescent particles in channel illuminated from both sides.

hard drive for further analysis.

The tracking algorithm also analyzed data obtained from observing the bubbles. It provided average gas phase parameters: bubble centroid velocity, fluctuations in the velocity (from RMS), void fraction, bubble size, and the Reynolds stresses. As the name suggests, shadowgraphy is implemented by casting a shadow around the bubble. It is accomplished by illuminating the flow with a light source such as halogen lamps or LEDs. In this study, a halogen lamp was employed. The illumination was strong and a diffuser plate was required to lower the intensity of the light so as to have a quality image. When light is incident on the bubble from behind, a shadow will be caused on the bubble due to refraction and reflection because water has a higher refractive index than air. In the images, the majority of the bubble results in a dark surface with a bright background. Using common image processing techniques, the image background can be removed leaving only the bubbles. This allows for the individual tracking of the bubbles. For shadowgraphy the camera was not synchronized to the illumination source. One signal was sufficient to trigger the camera and capture two consecutive images at 1000 fps. The camera was triggered every 0.2 seconds to ensure new bubble samples as in the case of PTV.

The calibration for PTV and shadowgraphy was accomplished by inserting a grid into the channel (Fig. 11). Images of the grid obtained from the camera assisted in converting between pixels and millimeters since the quantitative information provided by the tracking algorithm was presented in pixels. The conversion of one pixel to 0.024 mm was calculated using the calibration grid images.

It should be mentioned that the frame rate was not chosen randomly. Although 500 fps would not drastically affect the shadowgraphy analysis, results from previous experiments showed large displacement occurring in the region with liquid motion. This is not desired because it would lead to large velocity vectors which would require a large search area in the tracking algorithm. As a result, more computing time would be needed. In contrast if the measurements are taken with a larger frame rate i.e. 2000 fps, the small particle displacement in the tracking algorithm would produce erroneous velocity vectors. Therefore, 1000 fps was chosen for all PTV and shadowgraphy measurements for this study.

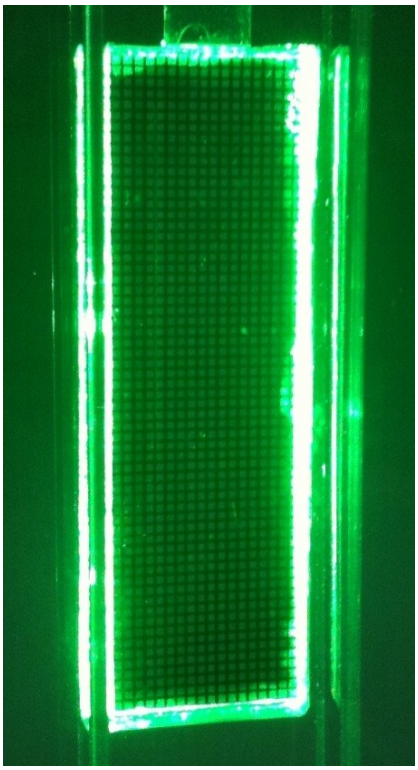

Figure 11: Calibration grid inserted in channel to compute the pixel to mm conversion.

CHAPTER III

DATA PROCESSING

Data processing after measurements were taken involved many procedures before the final results were obtained. The following sections will explain the procedures for each method and how they were performed.

3.1 Optical probe

Data processing for the optical probe did not include any difficult procedures. After collecting the data for 16 positions in the channel (total files = 160), the files were automatically saved in the folder specified in the software. Then a batch processing file was created including all 160 data files. When the batch file was executed by the probe software, each individual file was read and all data was extracted. Once the batch process was finished the software provided an Excel file with all the quantitative information from each individual data file, which was convenient for further processing. Next, the data was sorted into 16 sections of ten data lines (ten measurements were taken for each position in the channel) and all parameters were obtained and plotted from this file. From each section, the average value and standard deviation were calculated. The average value was required to make the plots, and the standard deviation provided the uncertainty in the values. It should be mentioned that the dual tip probe provided the void fraction and bubble frequency for each tip. When the plots of the two quantities are shown, it is the average value calculated from the two tips.

3.2 PTV data

A typical image acquired from the PTV method is shown in Fig. 12. The images were used in the tracking algorithm without any image processing. The full image was not tracked due to the dark corners resulting from the lens mounted on the camera. The lens size was smaller than the camera detector array. Therefore, the corners in the region were not captured. The central region was selected from the image to observe the flow without any hindrances. The dotted section in Fig.12 represents the 2.2 cm x 1.5 cm region shown in Fig. 7. This guaranteed that the analysis performed would cover all parts of that region. It was necessary to have a visibly clear portion to obtain an accurate distribution across the channel. The next step was to detect the particles in the specified region which comprised of many variables affecting the particle detection. The fluorescent particles were small and were considered to be the centroids themselves (not the case for shadowgraphy). The grayscale level of an image goes from 0 (completely black) to 255 (completely white). A grayscale level of 10 was determined to be sufficient for the PTV images, meaning that any pixel with a grayscale value of 10 or greater was detected as a particle. Afterwards, six additional variables remained to be defined for the particle detection.

A mask correlation technique implemented by the algorithm for particle detection comprised of six variables. The correlation technique generated an image template of an ideal particle. The algorithm searched for particles throughout the image using the template. Three shape modifying coefficients and the particle radius created the ideal particle template. Once the parameters had been defined for the ideal template,

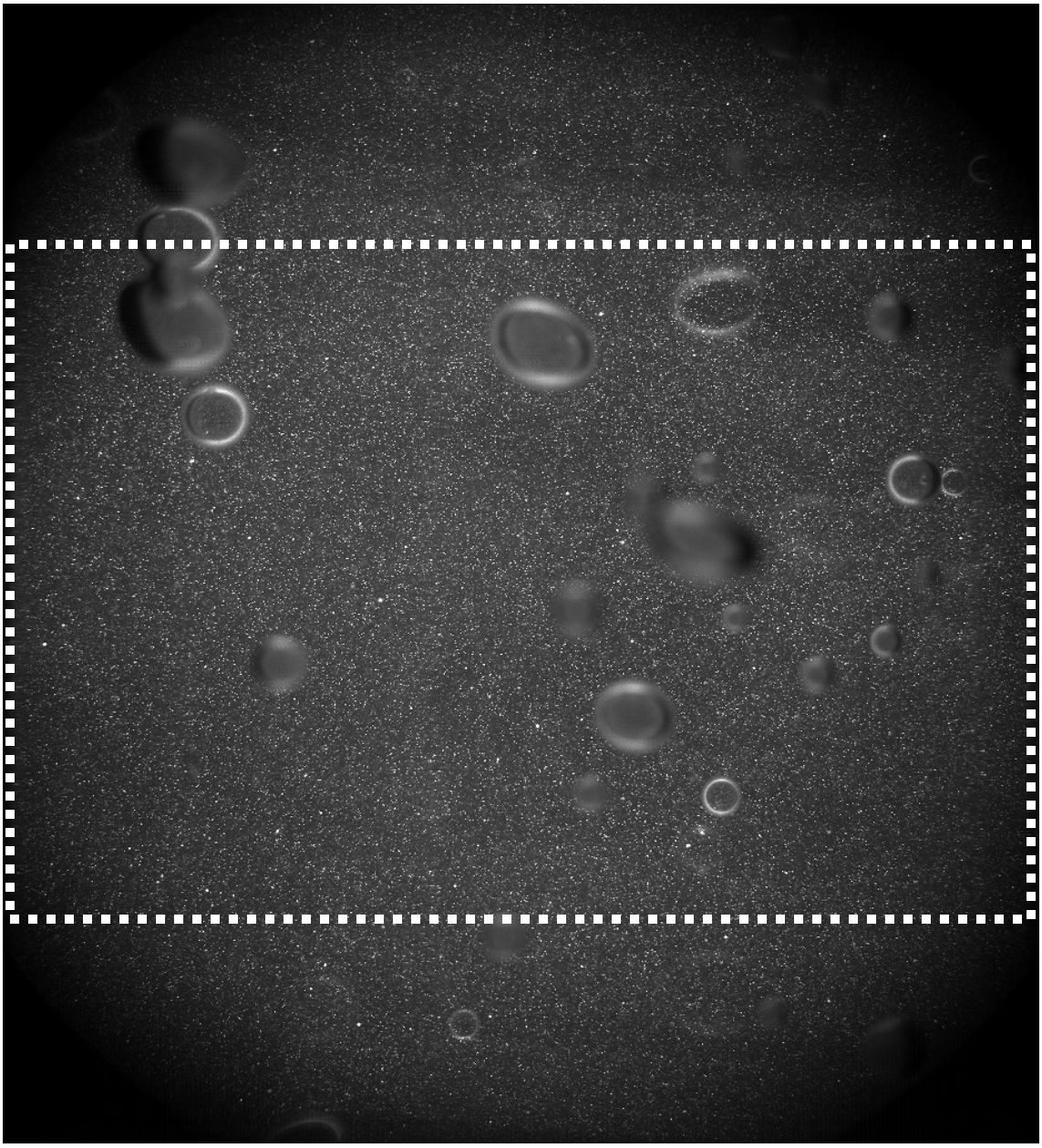

Figure 12: A PTV image from j_g = 2.5 mm/s case in region 1. The dotted box represents the approximate region considered for the particle tracking.

a cross-correlation (CC) threshold entered by the user determined a best fit between the ideal image template and the actual particle in the image. The CC threshold varied from

0 to 1. A CC threshold of 0 meant that all particles with the given radius and shape modifying coefficients were detected, whether or not they matched the ideal template. On the other hand, a CC threshold of 1 meant that only those particles having an exact match with the ideal template were detected. When the particle detection conditions were finally set, tracking of the images was possible. The tracking used two different windows to track the particles between consecutive images. First, the candidate window was fixed in the next image around the position of the particle in the current image and contained all the possible candidate particles. Afterwards, a correlation window was set around the current particle and each candidate particle. The final step in the particle tracking was performed by comparing the current particle and the possible candidate particles using the CC threshold (different from the one used in particle detection). The same criterion of 0 to 1 was applied in the tracking CC threshold as it was in the detection CC threshold. The straddling capability of the tracking program was employed since every image pair was tracked.

Output files from the tracking algorithm saved automatically as dat files in the same location as the images. The files were required for the next process: data filtering. The filtering program was separate from the tracking program. The main purpose was to filter out the incorrect data in the dat files using statistical methods. The first step for data filtering was defining the filtering region which was the same entered in the tracking program. The second step involved sectioning the region into different columns (on the horizontal axis). All procedures were performed on each column for all the images. The average of the original dat files was calculated and a range of values two

standard deviations (2σ) from the average were obtained. The average quantity ($\bar{a}$) was calculated as

$$\overline{a} = \frac{1}{N}\sum_{i=1}^{N} a_i \tag{5}$$

where a represents the component of the velocity (u or v), a_i the instantaneous velocity, and N the total number of vectors in the column. Afterwards, each instantaneous velocity was compared to the range of 2σ values. The quantity was discarded if the value was not contained within the range. The filtered velocities (those within the range) were used to calculate a new average, which provided the velocity distributions and other parameters. The RMS and Reynolds stresses were based on the new filtered average and each instantaneous velocity. The RMS was calculated as

$$RMS = \sqrt{\frac{1}{N}\sum_{i=1}^{N}(a_i - \overline{a})^2} \tag{6}$$

The average Reynolds stresses ($u'v'$) were calculated similarly using the individual fluctuations of each component:

$$u'v' = \frac{1}{N}\sum_{i=1}^{N}(u_i - \overline{u})(v_i - \overline{v}) \tag{7}$$

The overall process is graphically shown in Fig. 13.

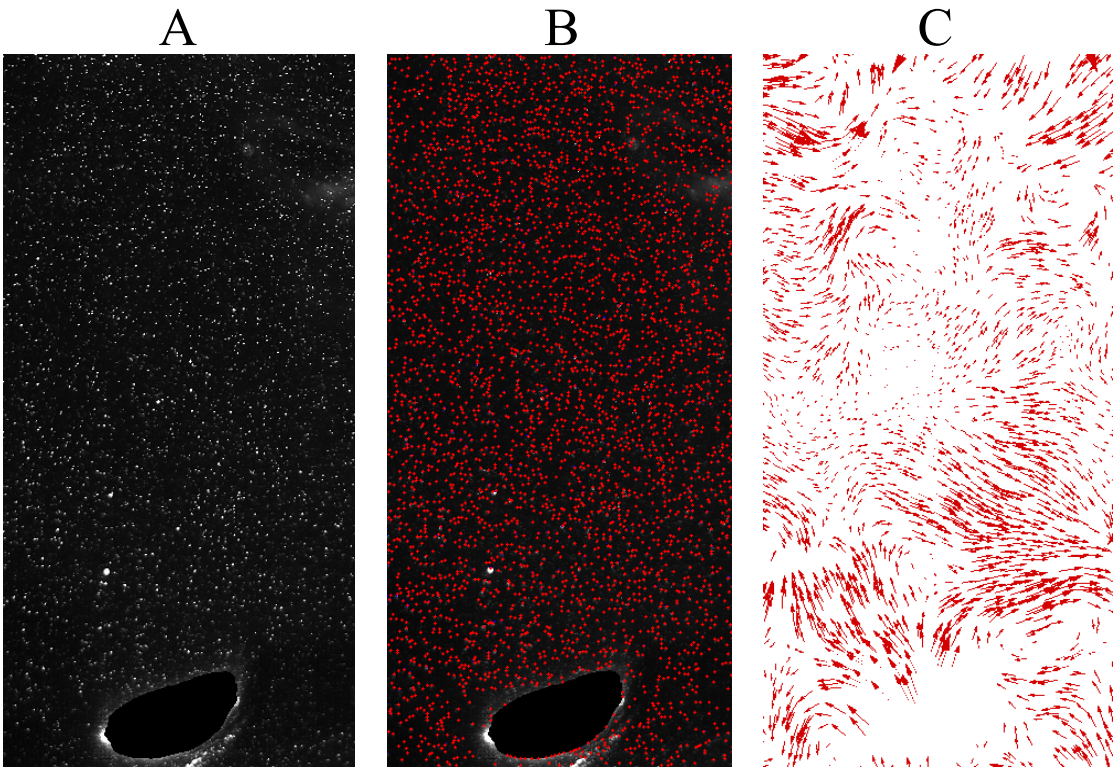

Figure 13: Process for PTV images: A) raw image, B) raw image with particle detection, C) velocity vector field after tracking and filtering.

3.3 Shadowgraphy data

The shadowgraphy images used in the tracking algorithm required processing in order to have only bubbles in the images. All images including the background were inverted. It was necessary to do so because the tracking program based particle detection on the grayscale level. The detection of the particle will be easier if it has a high grayscale level (closer to white). The bubbles in the original images were dark, and inverting the images made them closer to white. The inverted background (image of channel with no flow) was subtracted from the inverted shadowgraphy image to give the

final processed image employed in the tracking program. A section similar in size to the dotted section shown in Fig. 12 was considered for shadowgraphy in the analysis of the velocity fluctuations and Reynolds stresses. Since a comparison was to be made between the optical probe and shadowgraphy, the right half of the channel was considered for the analysis of the remaining shadowgraphy parameters (bubble centroid velocity, void fraction, and size). The tracking procedure used in PTV was the same applied for the shadowgraphy analysis. The centroid location detected the full bubble and estimated the center. It was sufficient for the detection since the bubbles were considered to be the particles themselves in this case. Therefore, applying the mask correlation technique was not necessary for shadowgraphy. Afterwards, the tracking was performed in the same way as in PTV, although the candidate window had to be increased to a larger size due to the rapid movement of the bubbles between images. The filtering was performed in the same method as mentioned in the PTV section once the tracking of the bubbles was complete. The filtering parameters were the same for both techniques. The overall process is graphically shown in Fig. 14.

3.4 Uncertainty quantification

Quantifying the uncertainty (error) in measurements is an essential part of the results. It was desired to have an estimation of uncertainty in the results. The error was obtained in a similar manner for the methods implementing the tracking algorithm (PTV and shadowgraphy) and the optical probe. The uncertainty for the optical probe was calculated by taking the standard deviation from each set of 10 measurements for each

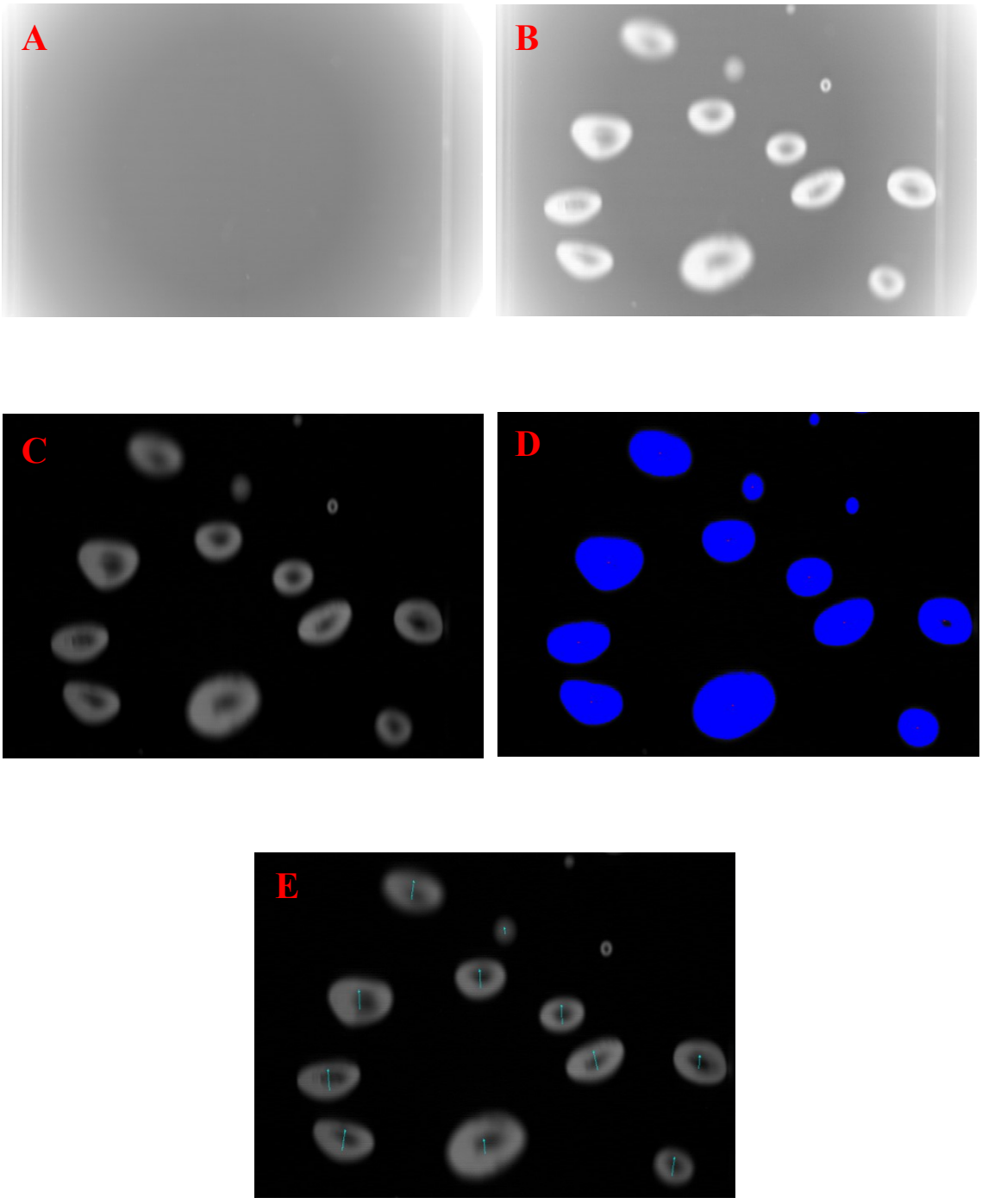

Figure 14: Process for tracking the shadowgraphy images: A) inverted background, B) inverted image, C) processed image, D) centroid location, E) bubble tracking.

parameter (void fraction, interface velocity, etc.). The standard deviation provided the fluctuation from the average value. Since 20 minutes of measurements were taken for each data point in the channel, it was assumed that the standard deviation was a reliable approximation for the uncertainty in the measurements. The error for PTV and shadowgraphy was also calculated using the standard deviation. The shadowgraphy data consisted of five sets and the standard deviation of each value for each parameter was calculated from the sets. Since each set of data contained 10,918 images (total 54,590 for each flow rate) it was assumed that five data sets were sufficient to approximate the uncertainty in each parameter for shadowgraphy. On the other hand, only one data set was taken for PTV measurements. The tracking performed from one PTV image-pair resulted in approximately 15,000 velocity vectors. Therefore, one data set was sectioned into five sub-data sets and a similar error analysis performed in shadowgraphy was applied to PTV.

CHAPTER IV

RESULTS AND DISCUSSION

In this section the results obtained from the experiment will be shown and explained. Before the results are discussed, knowledge gained from previous experiments pertaining to capturing images of the flow and discrepancies between different methods will be mentioned.

4.1 Experience from previous experiments

4.1.1 Optimizing time interval between image pairs

Prior to beginning the current experiment, time was invested on a similar experiment performed previously with the same apparatus. Three gas flow rates (large, medium, small), different from those used in the current experiment, were inserted into the channel. Only shadowgraphy and the optical probe were implemented, but the analysis focused on the shadowgraphy method. The purpose of the study was to find the optimal time between images that would result in less fluctuating profiles obtained from the tracking algorithm. When the experiment was initiated the conventional procedure of obtaining the images was implemented to obtain results. The images for all three flow rates were recorded continuously at 1000 fps resulting in 10,918 images (maximum internal camera memory). Figure 15 shows the bubble centroid velocity for all three flow rates as a function of the distance from the center of the channel (x = 0 mm). There are many fluctuations in each velocity profile and a clearly defined shape does not exist. In

order to reduce the fluctuations more frequent measurements were required. Usually, an increase in the sample number improves the statistics of the study. A bubble entering the region was tracked approximately 115 times before exiting. Thus, an effort was made to change the sample number of the bubbles – the bubbles that appeared in the image pairs. Tracking each bubble once instead of multiple times was desired.

Next, the images were captured in sets. The camera memory was partitioned into 64 sets each able to record 170 continuous images at 1000 fps. The camera was triggered every 15 seconds with a signal to record each set. This method ensured that a new sample of bubbles was observed after each set. Figure 16 shows the distribution resulting from this method. The results did not improve. Large fluctuations were still present in the profiles. Finally, it was decided to have a new sample of bubbles after each pair of images (it is required to have at least two consecutive images for tracking purposes). Now, the camera was triggered to capture only two images every 0.2 seconds because it took approximately 0.115 seconds (115 images at 1000 fps) to allow a completely new set of bubbles to enter the visualization region. Again, a total of 10,918 images were captured (5,459 image pairs). As Fig. 17 shows, this method significantly improved the velocity profiles. A more defined shape is present for all the flow rates, although some fluctuations are still present. Notice how the velocity distribution for the medium and large flow rates has changed positions from Fig. 15 to 17. The change indicates that using consecutive images may lead to an incorrect calculation since the velocity is in a different position in Fig. 17. Even though the profiles had improved, one set of 5,459 pairs was not sufficient. Five sets were captured (Fig. 18) in order to determine the

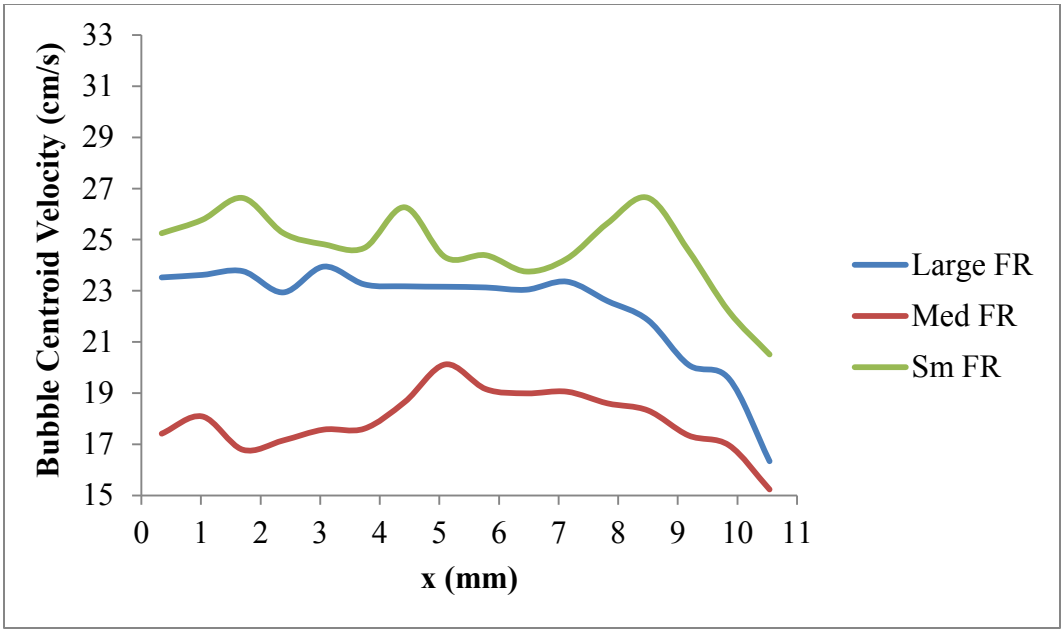

Figure 15: Velocity distribution in the channel for large, medium, and small flow rates (FR) from 10,918 consecutive images.

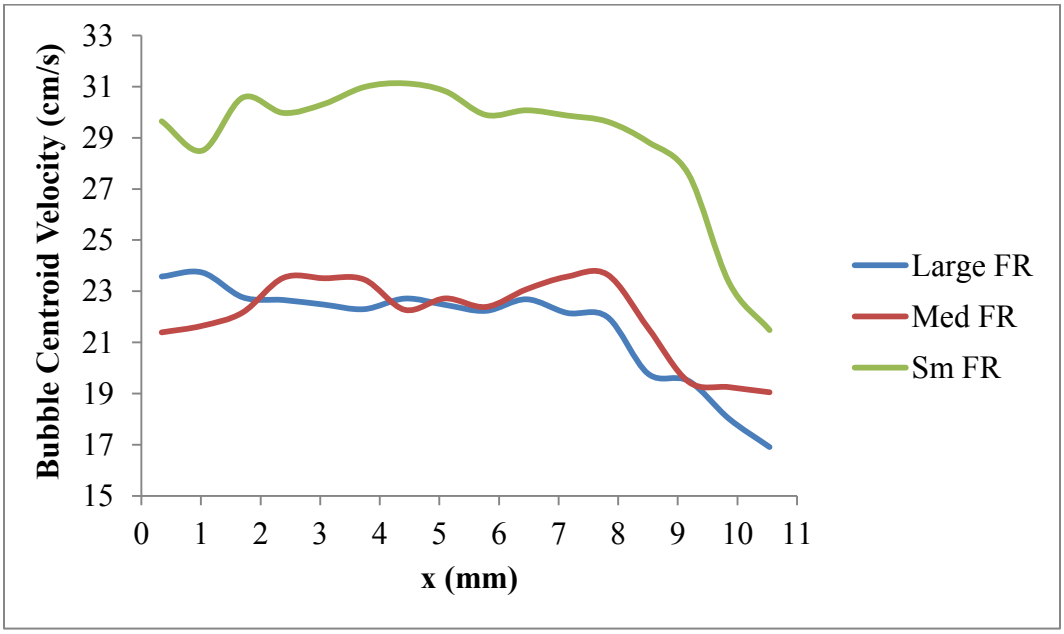

Figure 16: Velocity distribution in the channel for large, medium, and small flow rates (FR) from 64 sets of 170 consecutive images.

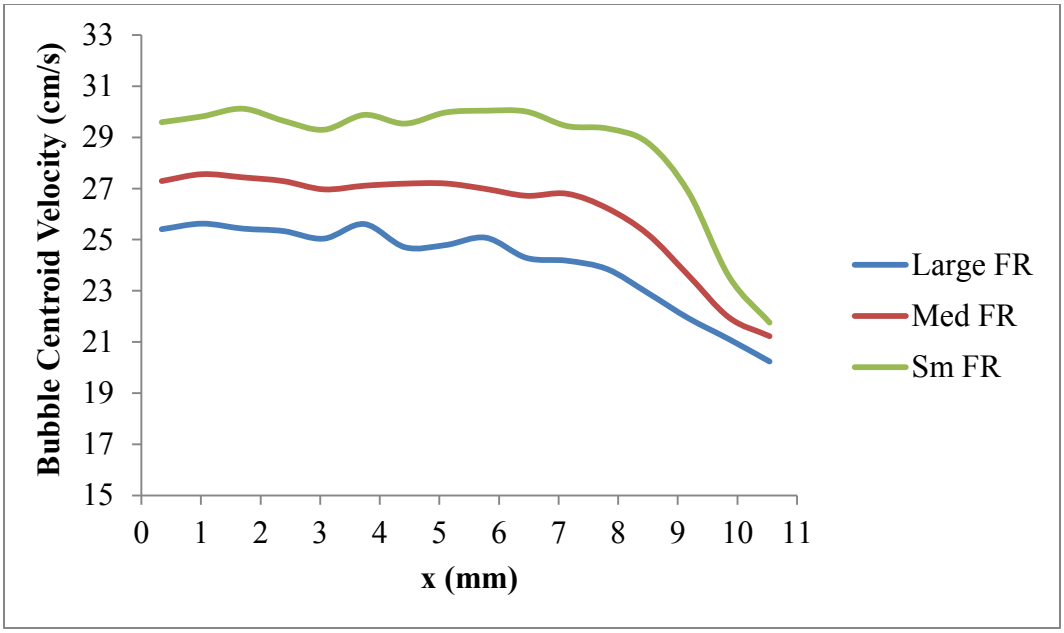

Figure 17: Velocity distribution in the channel for large, medium, and small flow rates (FR) from 10,918 images with an interval of 0.2 seconds between every two images.

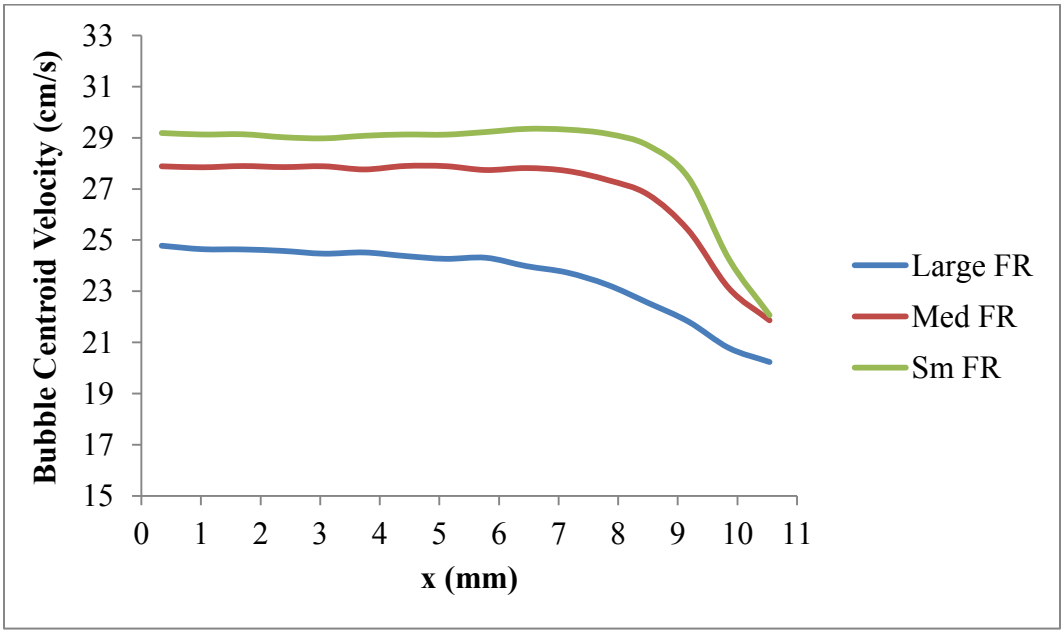

Figure 18: Velocity distribution in the channel for large, medium, and small flow rates (FR) from 54,590 images with an interval of 0.2 seconds between every two images.

uncertainty in the measurements. The tracking program analyzed five times the amount of data than before and performed the analysis on 54,590 images (27,295 image pairs) for each flow rate which immensely improved the velocity profiles. The fluctuations present in Fig. 17 have diminished and are no longer present in Fig. 18.

The sensitivity study vastly assisted in improving the velocity profiles, among other statistics not mentioned here. To obtain optimal results when using captured images, this study has shown it is recommended to have a different sample or inventory of bubbles present after each image pair. After performing this study, all the following measurements employing PTV and shadowgraphy had a sufficient time interval between image pairs to guarantee observation of a new set of bubbles.

4.1.2 Discrepancy between optical probe and shadowgraphy

Another important aspect was the discrepancy between the parameters provided by the optical probe and shadowgraphy. The optical probe measured higher velocity values and lower void fraction values than shadowgraphy. The two methods provide similar parameters through different techniques.

The optical probe calculates the bubble velocity based on the detection of the bubble surface, since it is the point of contact for the probe tip. The interface velocity is calculated by dividing the distance between the probe tips by the time it takes for the bubble surface to travel from one tip to the next, whereas shadowgraphy calculates the velocity by tracking the centroid of the bubble. Furthermore, the probe is a point measurement technique while shadowgraphy is a 2-D method. The probe velocity

calculation presents a problem because the bubble surface is constantly deforming and deforms even further when the bubble interacts with the probe. On average the bubble centroid has a smaller displacement than does the bubble surface. Since the surface is moving faster than the centroid, the velocity resulting from the probe will be greater than the one resulting from shadowgraphy. In Fig. 19, two cases of bubble-probe interaction are shown. The bubble centroid and interface are shown separately in consecutive images A and B, while image C shows the two images (A and B) superimposed. Image C from both cases reveals the average axial displacement and a larger difference is seen for the bubble surface. Note that the squares in the images represent an approximate location of the bubble centroid and surface.

Shadowgraphy presents an issue calculating the velocity and void fraction due to a dimensional disagreement. The problem encountered in shadowgraphy is the representation of a 3-D region as a plane (2-D). The method captures all the bubbles in the region of interest (which is a volume) but shows a planar view of that region. Even though the velocity in the central plane of the channel is desired, the calculated velocity is an average of multiple planes throughout the channel where the bubbles exist. Due to this issue, the void fraction will be much greater when calculated by shadowgraphy because all the bubbles in the 3-D volume are collapsed into a 2-D image. For example, if there were only five bubbles in the plane of interest shadowgraphy images may show greater than ten bubbles. It is believed that the aforementioned phenomena cause the discrepancy between the two methods.

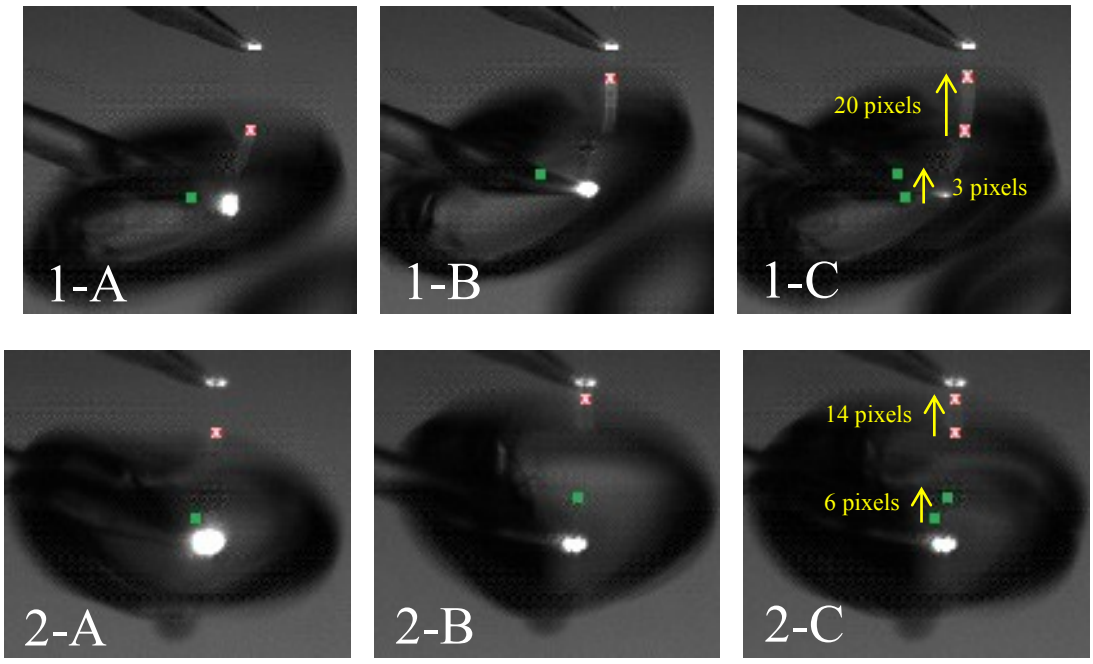

Figure 19: Two instances showing the difference in the movement of the bubble centroid( ) compared to the bubble surface closest to the probe tip ( )

4.2 Experimental results

Rather than show the data separately, the results from both sections will be shown. A general explanation of the results in the first region will be given, followed by a comparison for the two regions. In this manner any differences between the two regions will be evident.

4.2.1 Optical probe results

The optical probe provided gas phase parameters. Figures 20, 21, and 22 show the average void fraction distribution across the channel for the different flow rates. There is an increase in the void fraction closer to the wall than the center. This peaking

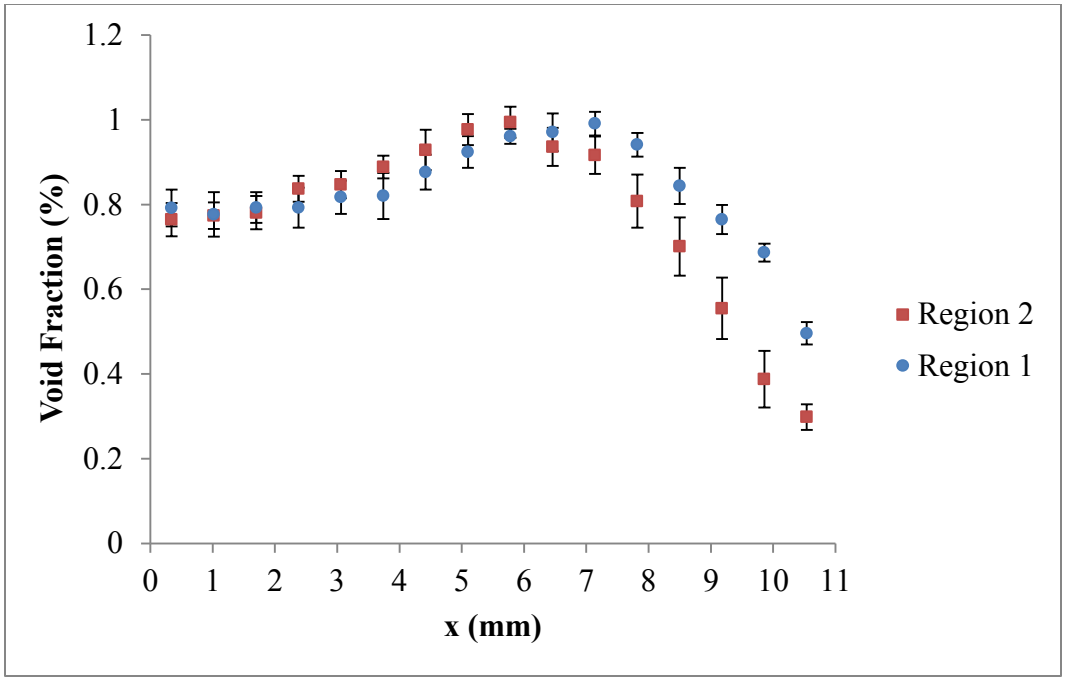

Figure 20: Average probe void fraction in both regions for j_g = 4.6 mm/s.

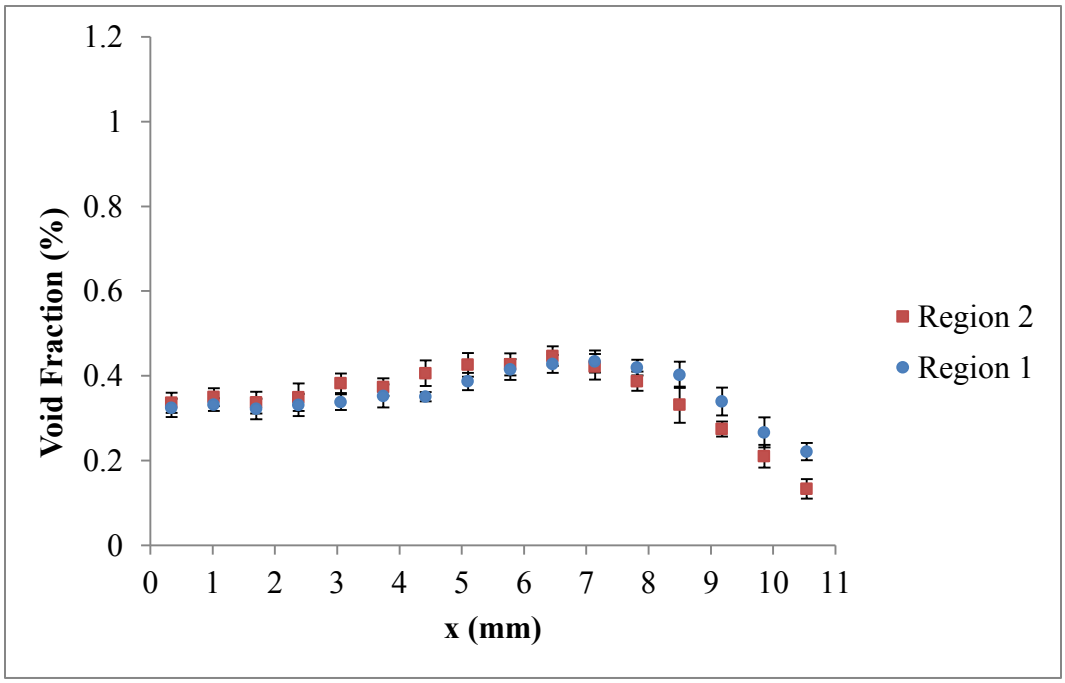

Figure 21: Average probe void fraction of both sections for j_g = 2.5 mm/s.

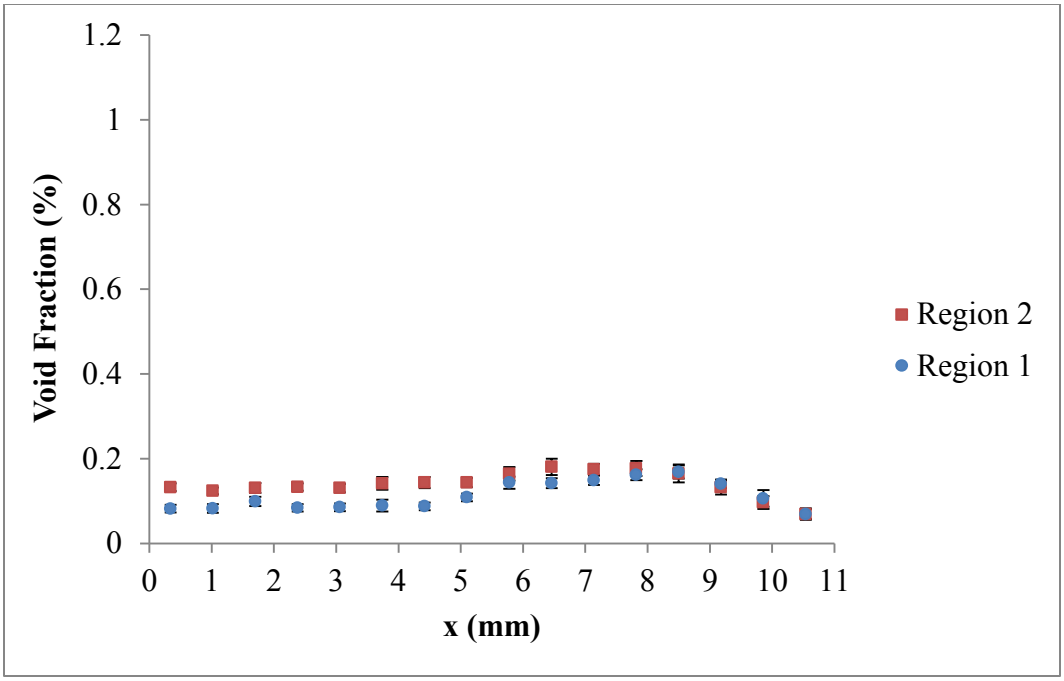

Figure 22: Average probe void fraction in both regions for j_g = 1.4 mm/s.

is due to the lift force that occurs close to the wall (Mudde et al., 2008). Low values of the void fraction were observed. The void fraction decreases when the flow rate is reduced, since the size and amount of bubbles become smaller in the channel. The bubble frequency (Figs. 23-25) displays a similar peaking effect found in the void fraction as the bubble concentration affects both parameters. Note that in Figs. 23-25, the bubble frequency is the average number of bubbles per minute. Therefore to obtain the total number of bubbles, the value must be multiplied by 20 (20 minutes of measurements were taken in each position).

The void fraction profile for both sections is very similar. For the high and medium flow rates the void fraction is within the error bars of both sections prior to the

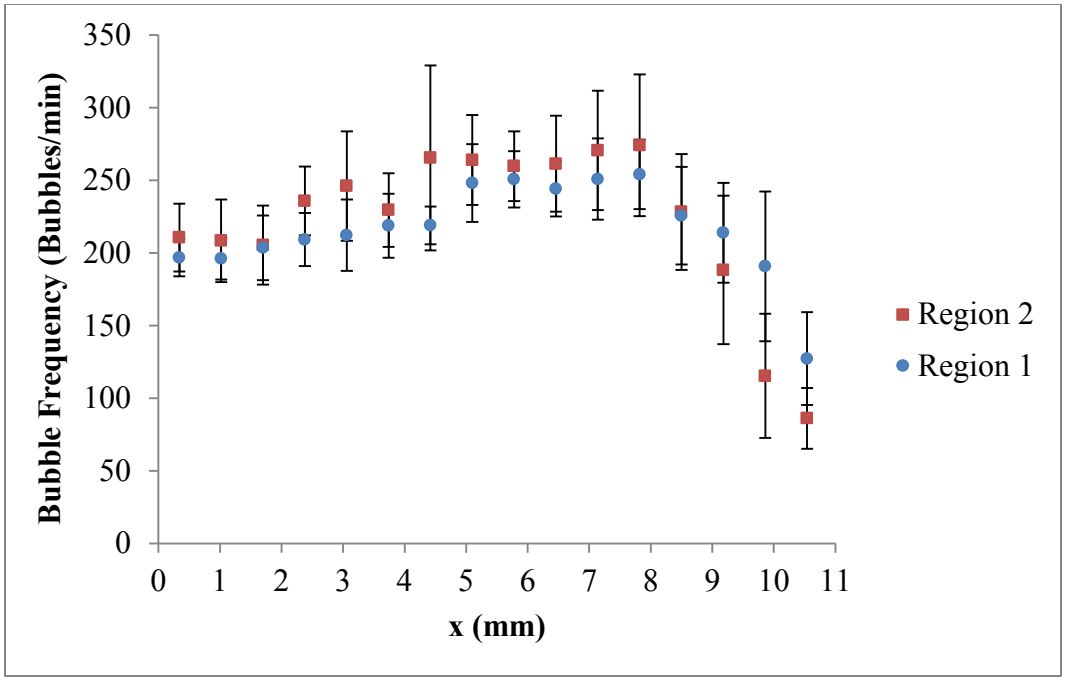

Figure 23: Average bubble frequency (per minute) in both regions for j_g = 4.6 mm/s.

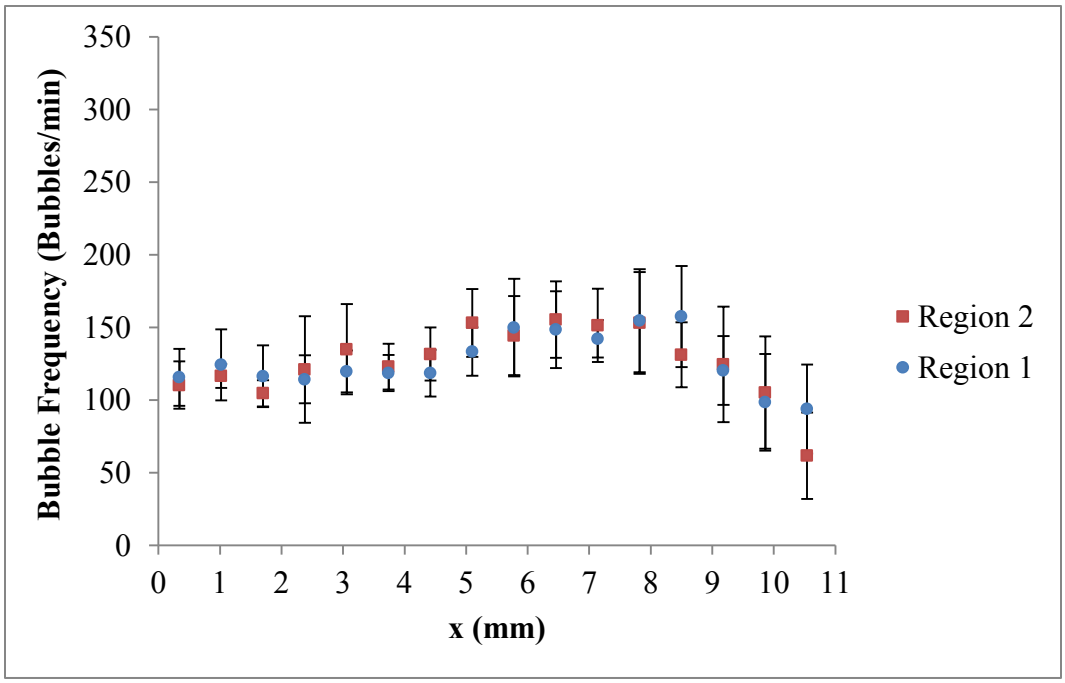

Figure 24: Average bubble frequency (per minute) in both regions for j_g = 2.5 mm/s.

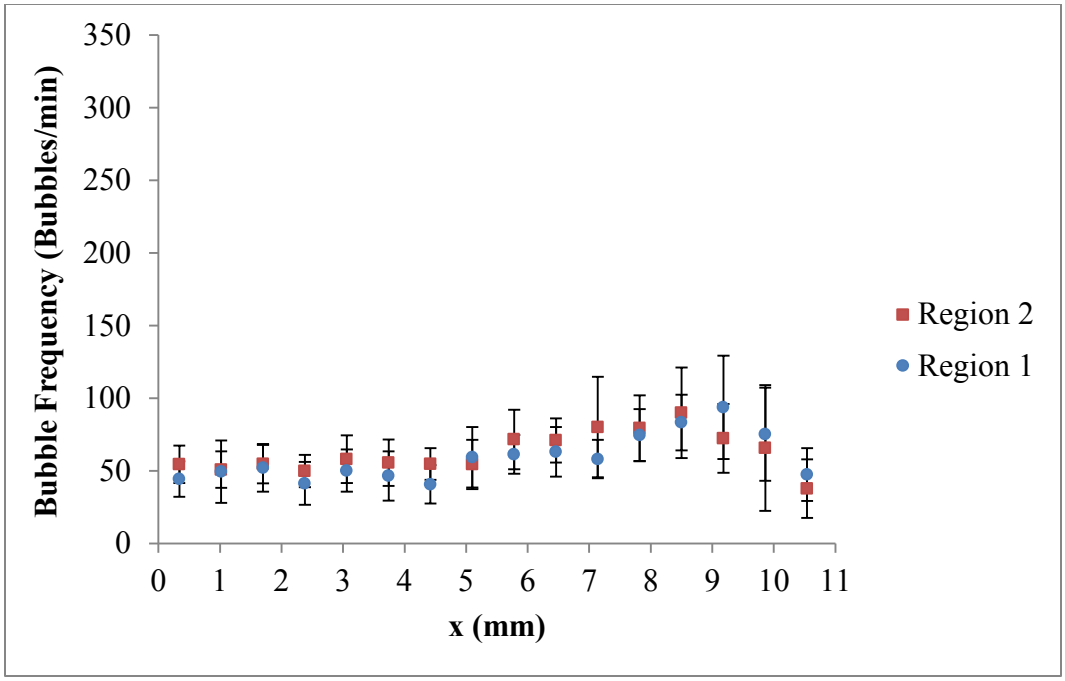

Figure 25: Average bubble frequency (per minute) in both regions for j_g = 1.4 mm/s.

peaking. After the peak, the Region 2 void fraction became lower than Region 1. On the other hand, the low flow rate case shows the void fraction to be within the error bars after the peak, but the Region 1 profile is lower than Region 2 before the peaking. The reason may be due to the variation in the range of the bubble frequency in a given point (note the error bar sizes if Figs. 23-25). Another factor affecting the difference in the measurements is the activation of the pores in the porous media. Even if the same flow rate is entering through the porous media, different pores will activate allowing bubbles to enter the channel in different locations. The change in the location of bubbles entering the channel became more severe as the flow rate was reduced. As for the bubble frequency both sections showed a similar profile for all three flow rates.

The time required for a bubble to travel from one probe tip to the next was termed the time of flight, as shown in Figs. 26-28. Observe the increase in the value as the distribution approaches the wall. The bubbles take a longer time to travel from one probe tip to the other when they are closer to the wall. A decrease in motion will occur from the bubble-wall interaction, causing the time of flight to increase. It was visually confirmed that the bubble motion was significantly reduced when they collided with the wall. According to the void fraction plots, bubble to bubble interactions will also occur because of the peaking near the wall and may be another reason why the time of flight increases. Since velocity is defined by the ratio of distance to time, the bubble interface

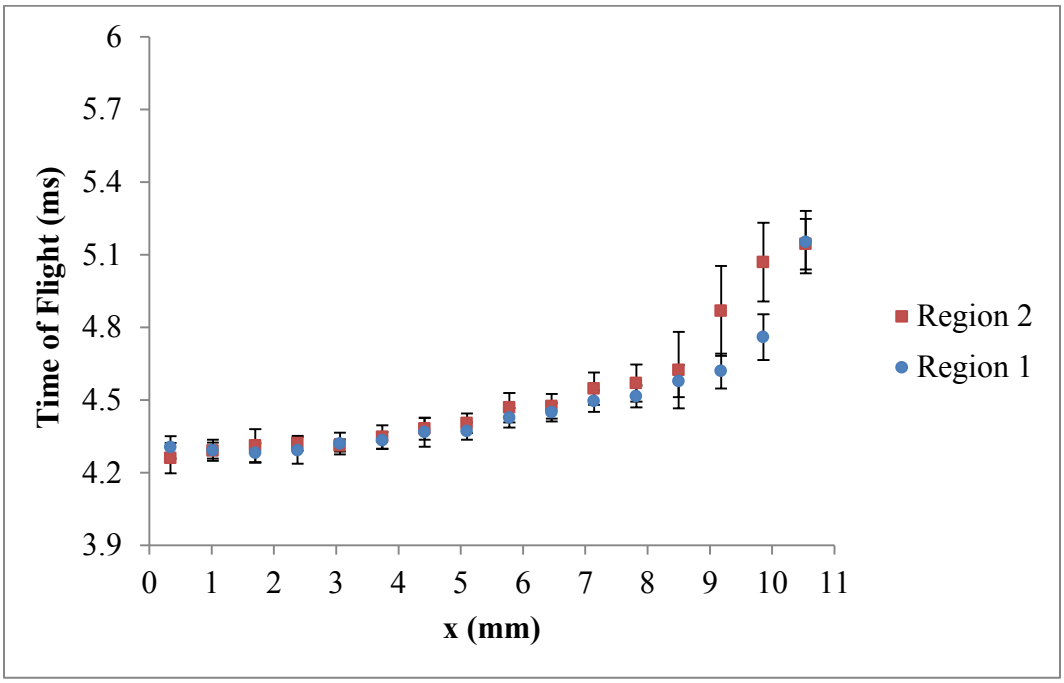

Figure 26: Average time of flight in both regions for j_g = 4.6 mm/s.

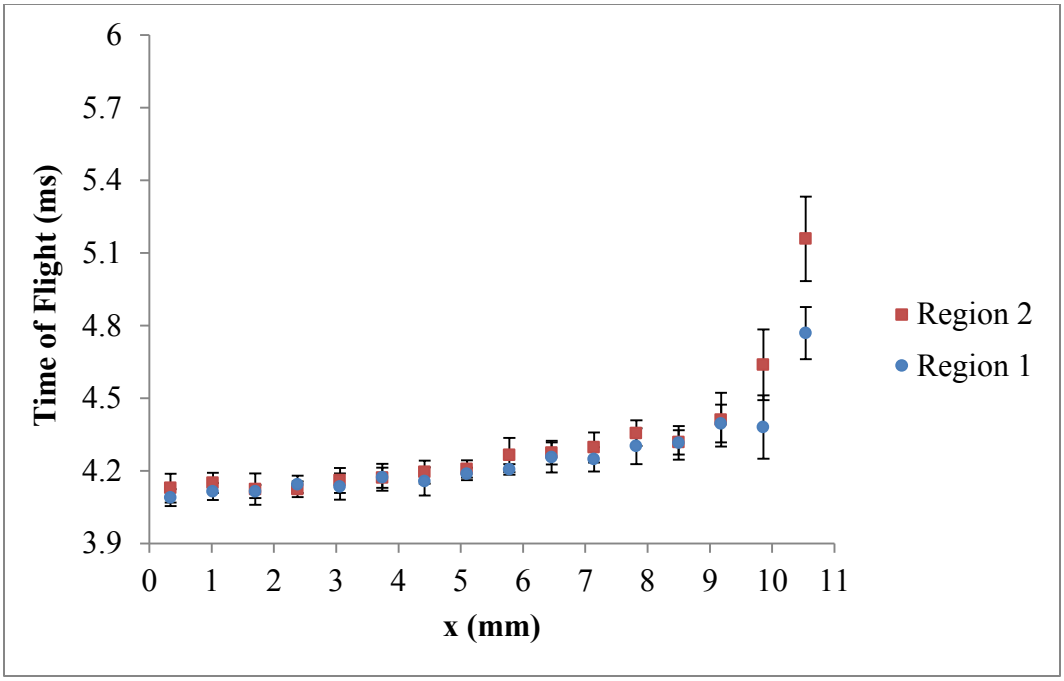

Figure 27: Average time of flight in both regions for j_g = 2.5 mm/s.

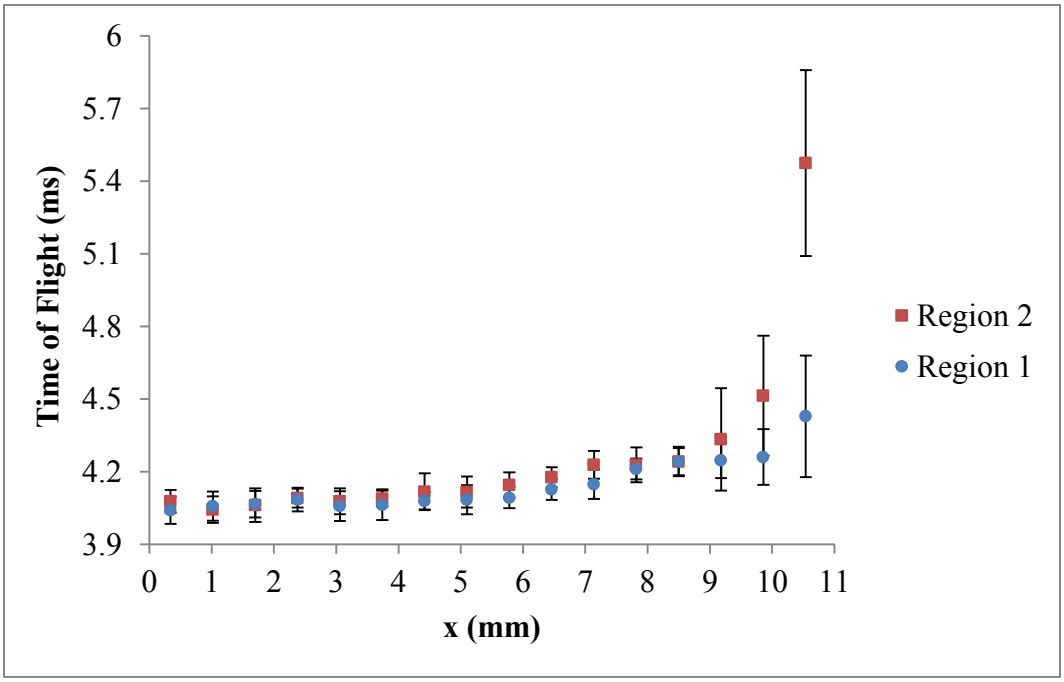

Figure 28: Average time of flight in both regions for j_g = 1.4 mm/s.

velocity (Figs. 29-31) profile will be the inverse of that shown in Figs. 26-28. The distance between the probe tips is fixed (1.4 mm) and the time of flight is the only variable affecting the velocity. As the time of flight increases the interface velocity will decrease. The same reasons in the case of the time of flight apply for the decrease in the interface velocity near the wall.

The time of flight and interface velocity distributions had similar profiles for both sections, except close to the wall. The figures show that as the flow rate is reduced the bubble interface takes a longer time to travel from one tip to the other for Region 2 results compared to Region 1. Therefore, the interfacial velocity is lower for Region 2.

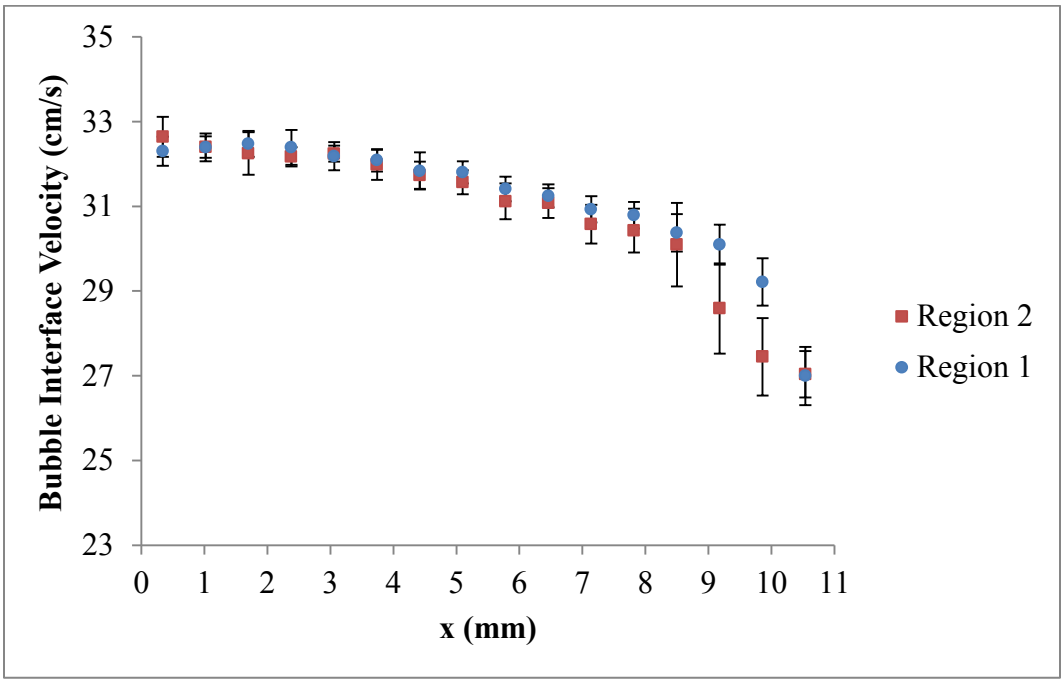

Figure 29: Average bubble interface velocity in both regions for j_g = 4.6 mm/s.

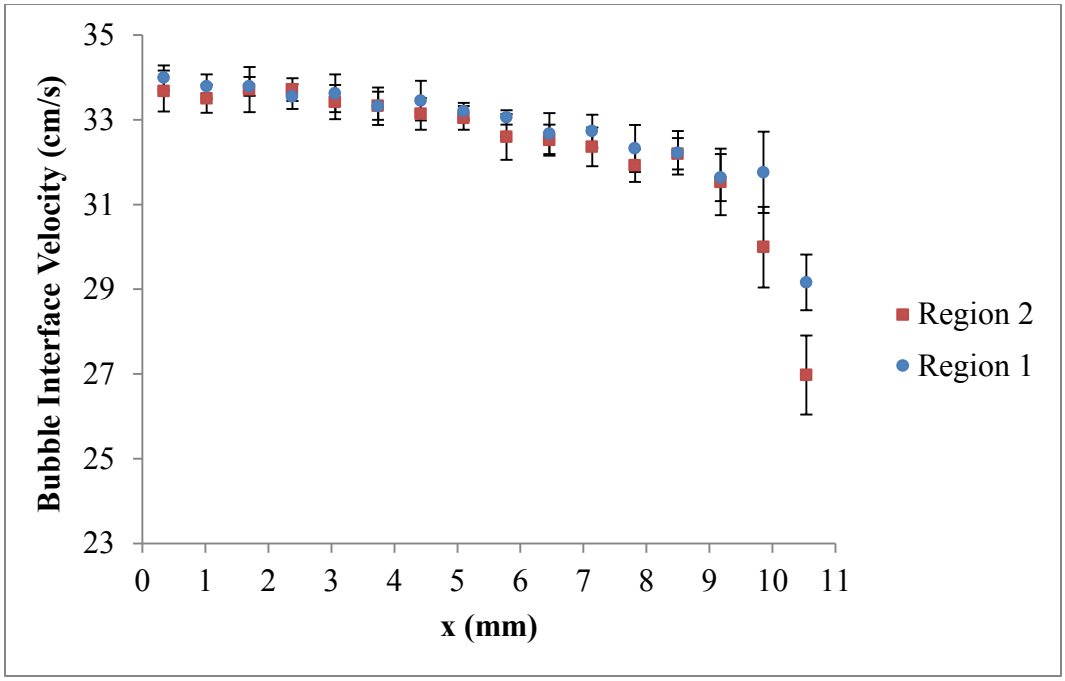

Figure 30: Average bubble interface velocity in both regions for j_g = 2.5 mm/s.

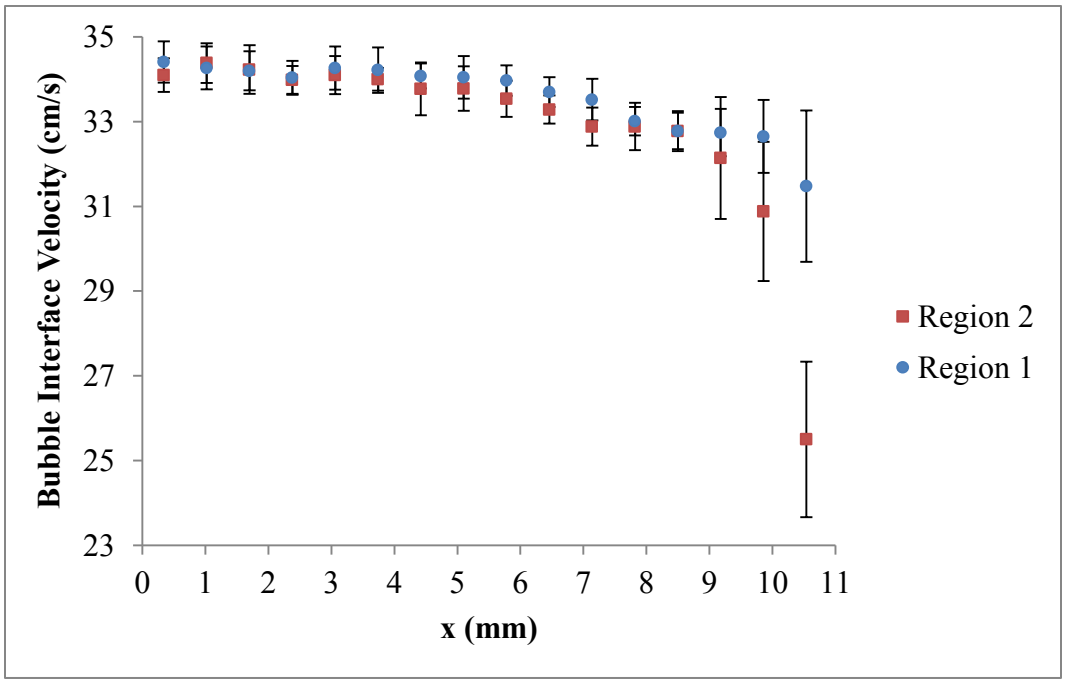

Figure 31: Average bubble interface velocity in both regions for j_g = 1.4 mm/s.

There may have been slow moving bubbles near the wall in the second region from the different pore activation, since slow moving bubbles would have a larger T_{flight}.

The average interface velocity increases with decreasing flow rate. The opposite may be expected as larger bubbles are thought to travel faster due to their size. However, the results show that larger bubbles have the lowest average velocity. This may be caused by surface deformations of the larger bubbles. Another explanation may come from the forces acting on the bubble. Larger bubbles have less surface tension (per volume) and are more buoyant compared to smaller bubbles. They oscillate more frequently than smaller bubbles and the surface is constantly deforming. Small bubbles do not have surface deformations on the same scale as do large bubbles. Although they are less buoyant, less frequent oscillations may allow them to travel faster. Both types of oscillations for the two bubble sizes were visually confirmed. It should be mentioned that the interface velocity trend from the different sized bubbles may be due to a certain size range present from the flow rates chosen for this experiment. From this study the results showed a greater interface velocity for smaller bubbles than for larger bubbles. This does not infer that if the flow rate is reduced further, bubbles smaller than the current size will travel faster. Similarly it does not infer that bubbles larger than their current size will travel slower if the flow rate is increased further.

Based on the void fraction and bubble frequency plots, the low bubble concentration close to the wall will increase the uncertainty in the interface velocity and the average uncertainty will increase with decreasing flow rate (notice overall increase on the error bar size on Figs. 29-31). Also note the large error bars on the last data points

for Fig. 31. As mentioned earlier, the pore activation affects the location of the bubble formation. Although the majority of the bubbles are formed in the center of the porous media, a random formation of the bubbles close to the wall was observed for the low flow rate case.

The Sauter mean diameter (Figs. 32-34) was not found to have any particular pattern as the flow rate decreased other than the decrease in the average size and increase in the average uncertainty. It was expected that the bubbles will become smaller as the flow rate was reduced, which is shown in the figures. The increase in the uncertainty implies the variation in the bubble size as the flow rate decreases.

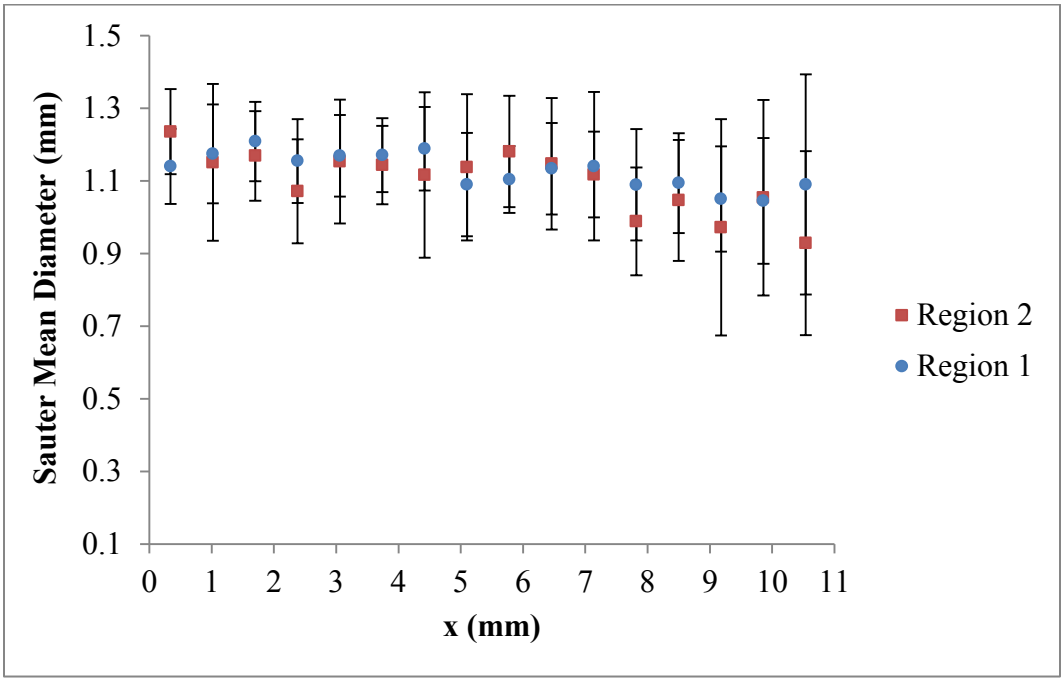

Figure 32: Average Sauter mean diameter in both regions for j_g = 4.6 mm/s.

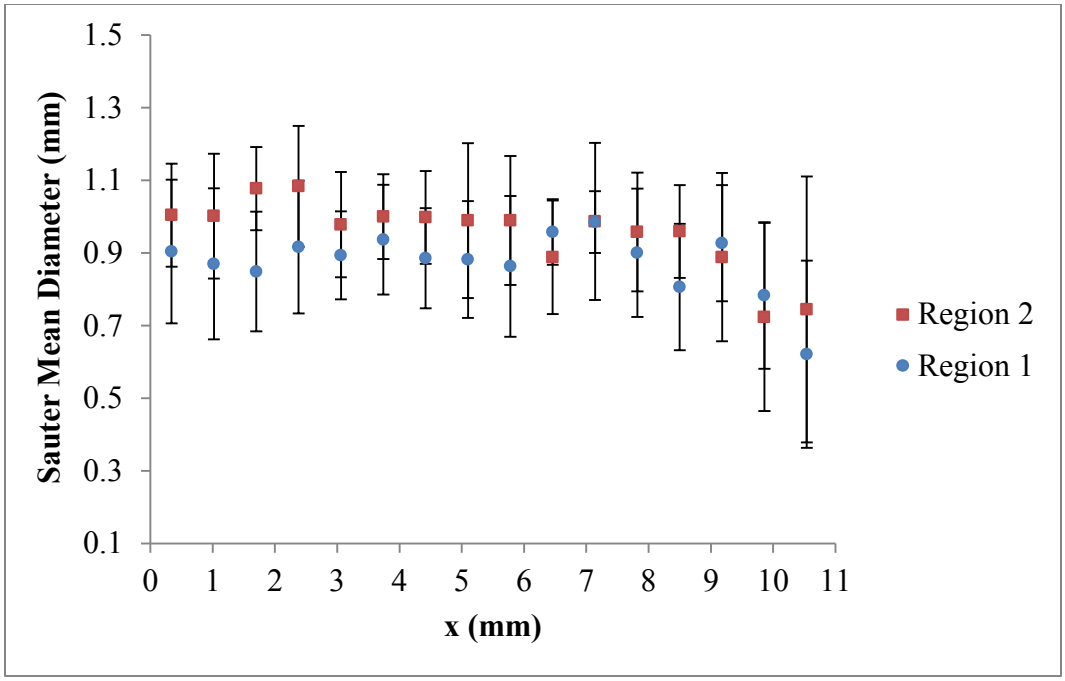

Figure 33: Average Sauter mean diameter in both regions for j_g = 2.5 mm/s.

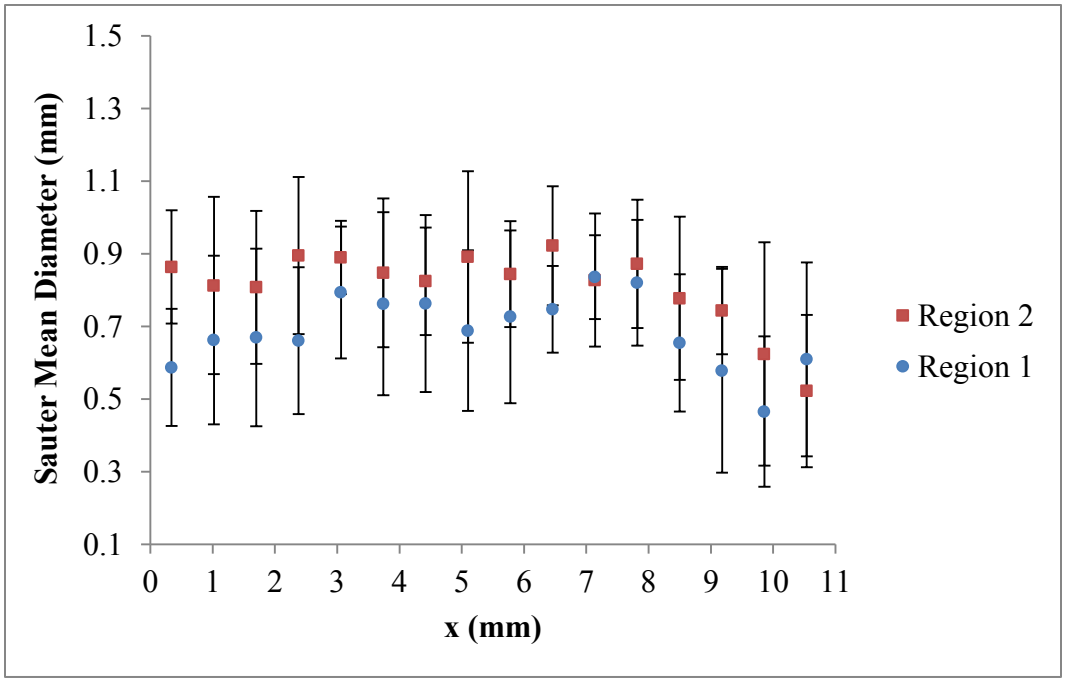

Figure 34: Average Sauter mean diameter in both regions for j_g = 1.4 mm/s.

4.2.2 Shadowgraphy results

Figures 35-37 show the average bubble centroid velocity distribution for the three flow rates. Note that the velocity profiles are increasing as the flow rate decreases (similar to bubble interface velocity from probe). The same explanation given for the optical probe can be applied here, although there is a dip in the profile for j_g = 1.4 mm/s. The dip in the center of the distribution can be attributed to the low amount of bubbles that were present in the center of the channel. In the small flow rate case many small bubbles ranging from approximately 360 – 480 μm emerged from the porous media and remained mainly in the center. Even if there are larger bubbles moving faster in the center of the channel, the tiny bubbles form a cluster with the larger bubbles and the cluster is tracked as one bubble. The tiny bubbles also formed clusters. The extremely slow velocity of the tiny bubbles reduced the average centroid velocity.

The velocity for both sections in all three plots has the same trend for the high and medium flow rates. The low flow rate shows an increase in the velocity for Region 2 near the center. Since the trend of increasing velocity is not found in Region 1 results for j_g = 1.4 mm/s and the only difference between the two regions is the position in the channel, the bubbles may not have been fully developed in the first region. Figures 35 and 36 show a relatively constant velocity in the center of the channel and all three figures show a decreasing velocity near the wall. Also, there seems to be a peaking effect in the velocity profiles. The velocity distribution for the large flow rate is slightly core-peaked and becomes more wall-peaked as the flow rate is reduced.

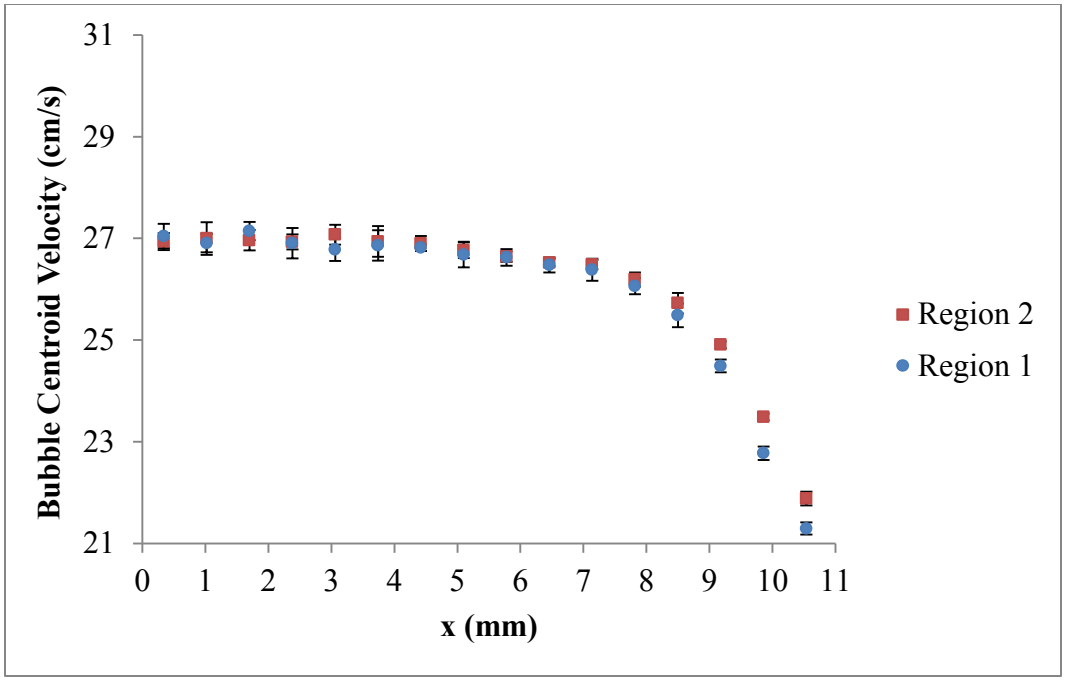

Figure 35: Average bubble centroid velocity in both regions for j_g = 4.6 mm/s.

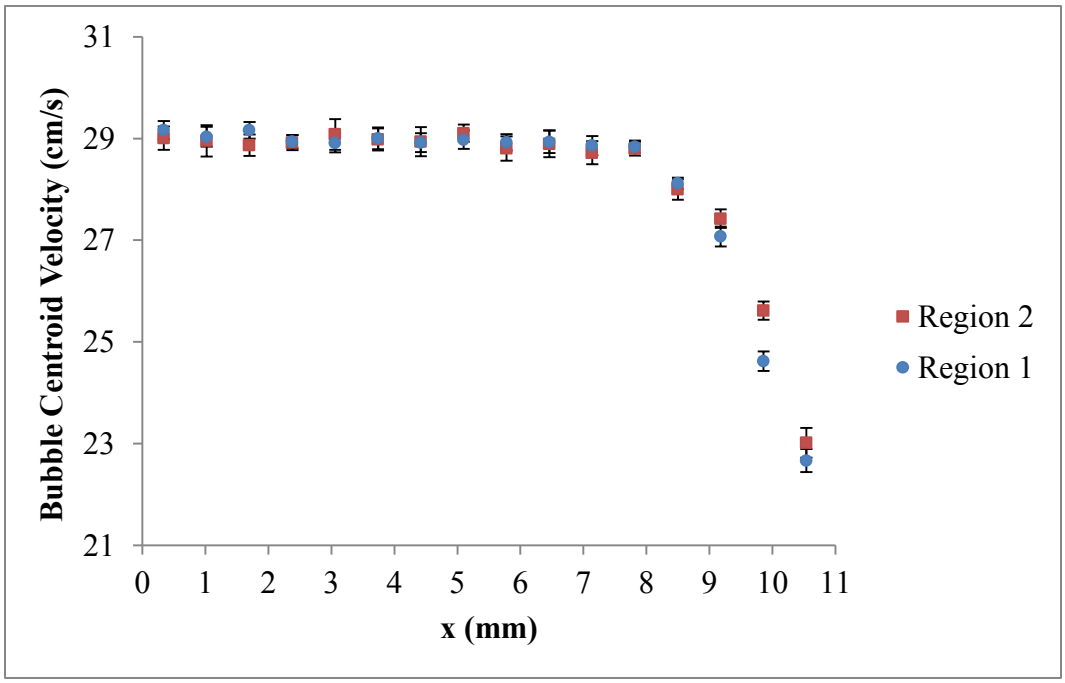

Figure 36: Average bubble centroid velocity in both regions for j_g = 2.5 mm/s.

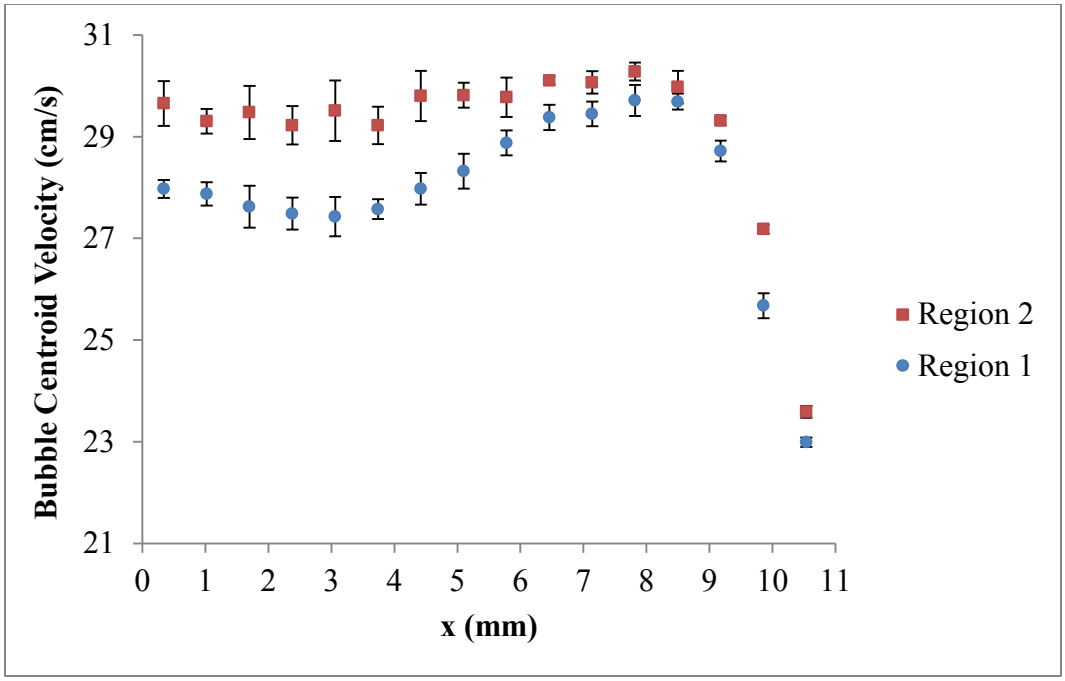

Figure 37: Average bubble centroid velocity in both regions for j_g = 1.4 mm/s.

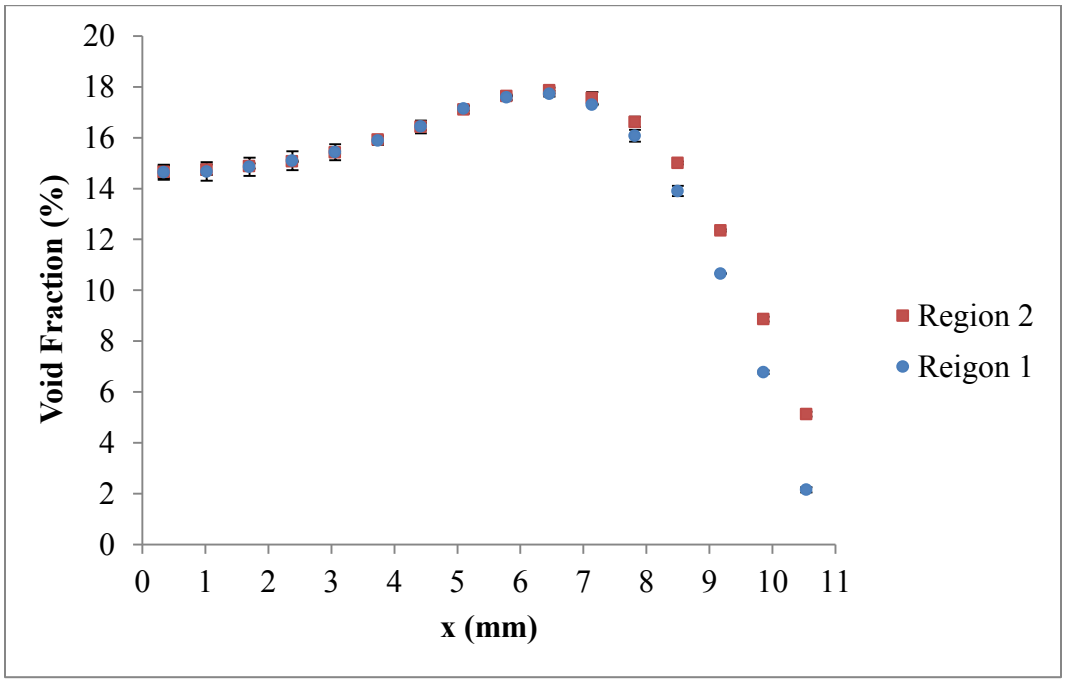

Figure 38: Average shadowgraphy void fraction in both regions for j_g = 4.6 mm/s.

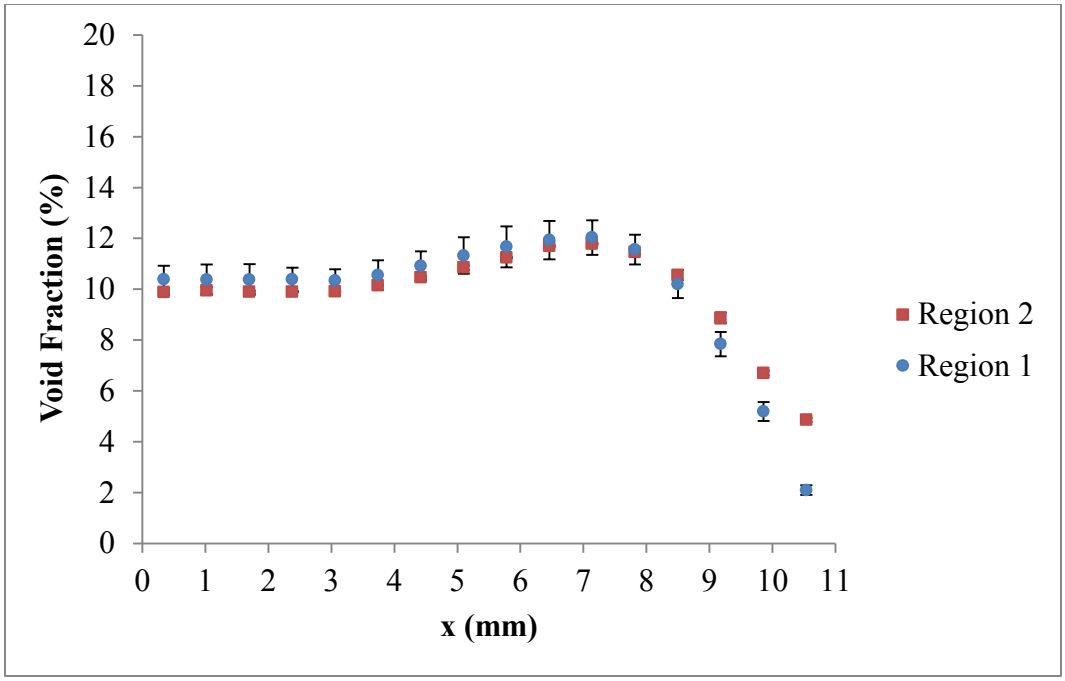

Figure 39: Average shadowgraphy void fraction in both regions for j_g = 2.5 mm/s.

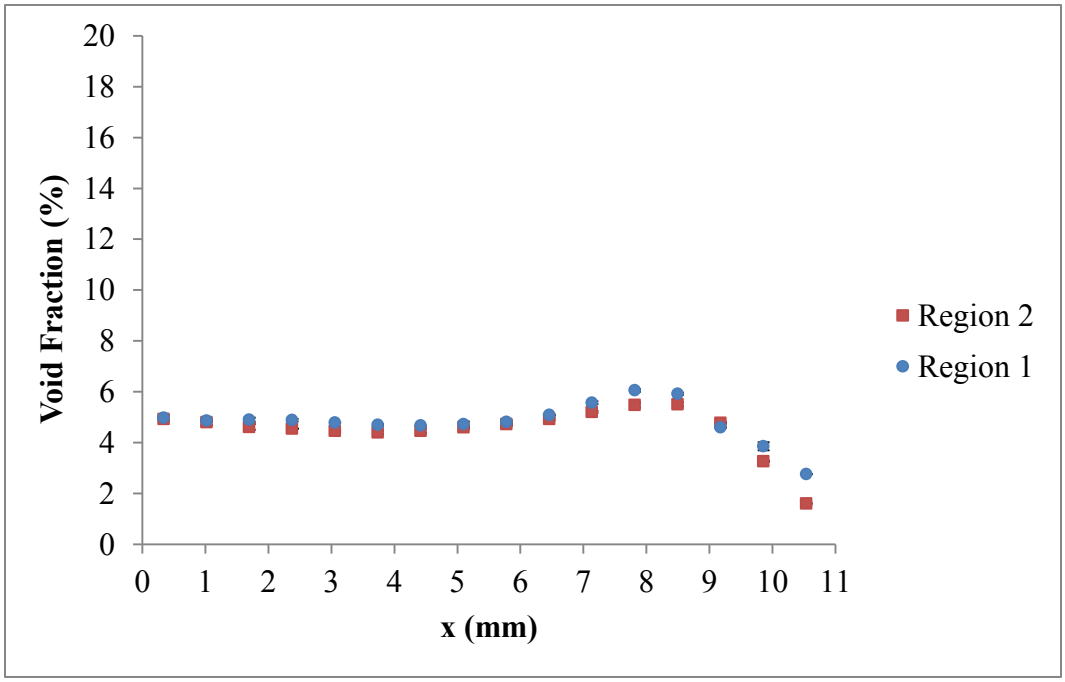

Figure 40: Average shadowgraphy void fraction in both regions for j_g = 1.4 mm/s.

The void fraction profiles provided by shadowgraphy are shown in Figs. 38-40. The distributions have higher magnitude than the ones obtained from the optical probe. The discrepancy regarding the dimensional disagreement causes the large difference in the void fraction. It can be seen from the figures that as the flow rate is decreased the distribution becomes more wall-peaked and the central region becomes flatter, meaning the bubble concentration in the center decreases. The profiles of the void fraction were found to be similar for all three flow rates in both regions.

Bubble sizes were also estimated from the shadowgraphy data (Figs. 41-43). The size was based on the assumption that the bubbles were spherical (circular in 2-D view). The figures show the size to decrease as the flow rate decreases, confirming that the

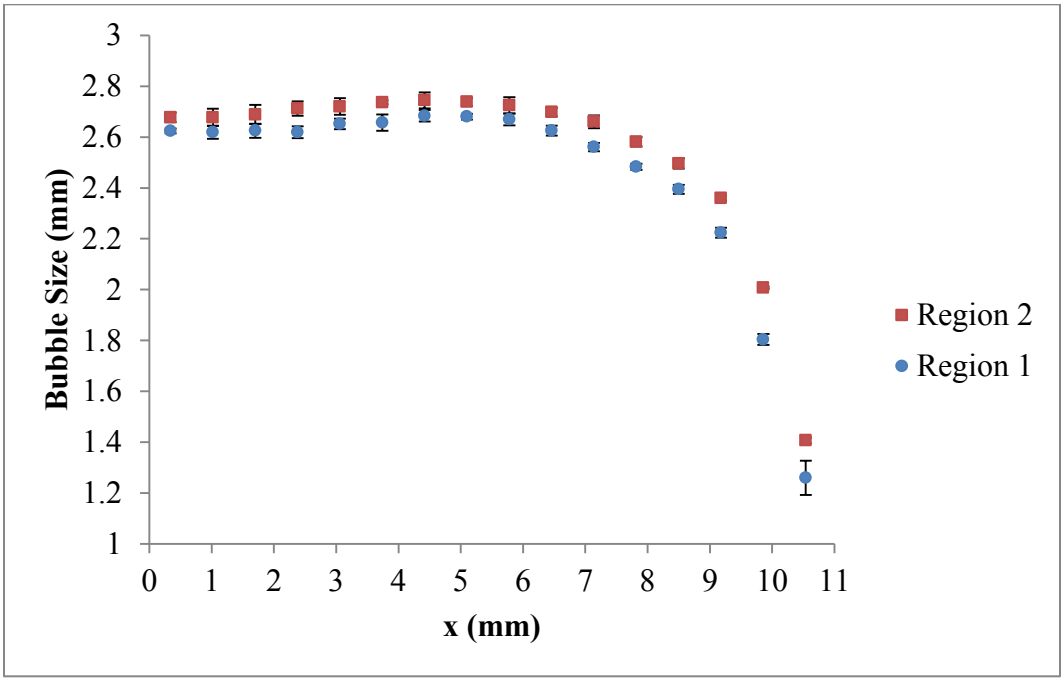

Figure 41: Average shadowgraphy bubble size in both regions for j_g = 4.6 mm/s.

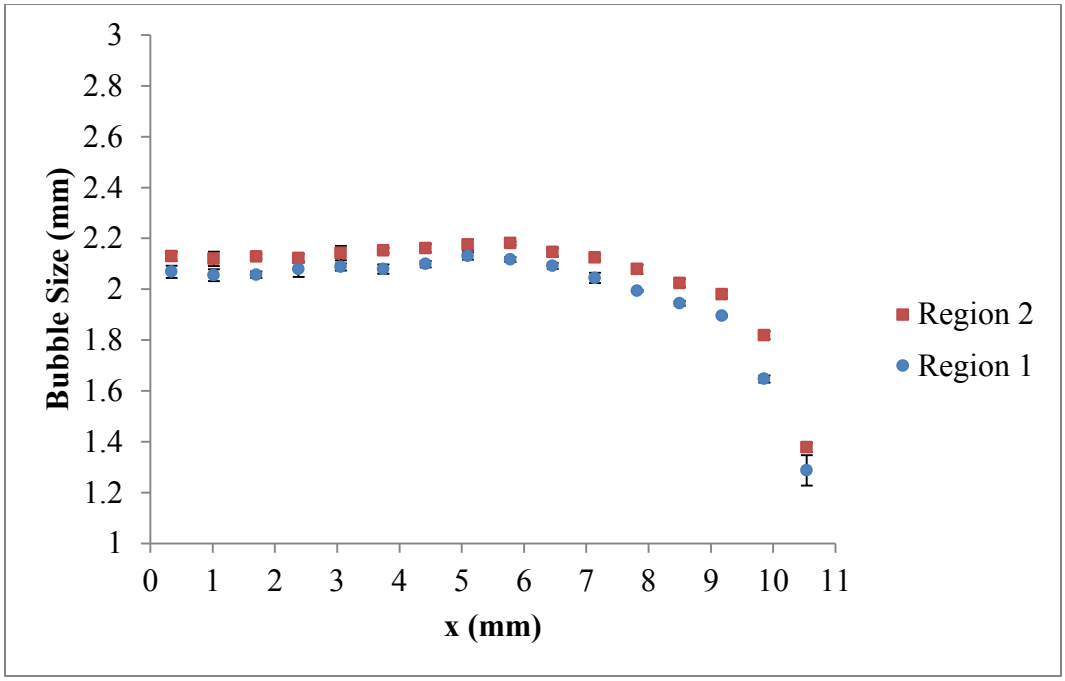

Figure 42: Average shadowgraphy bubble size in both regions for j_g = 2.5 mm/s.

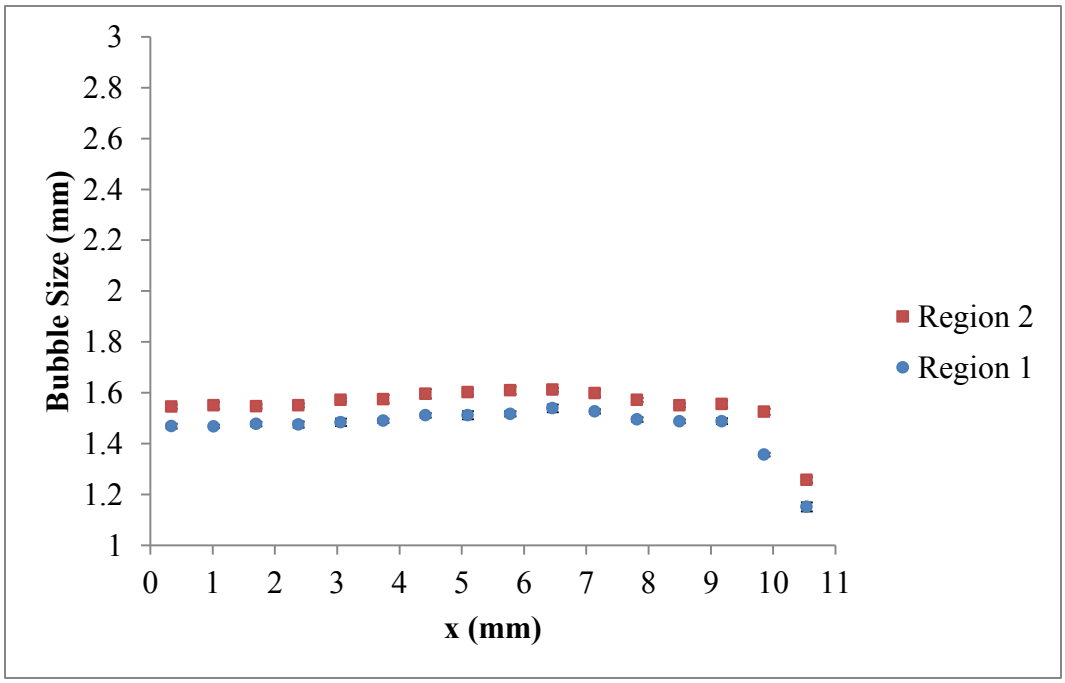

Figure 43: Average shadowgraphy bubble size in both regions for j_g = 1.4 mm/s.

bubbles become smaller as the flow rate is reduced. The same trend was seen in the Sauter mean diameter from the optical probe. Both regions exhibit a similar profile. For each flow rate, the size is fairly constant after which the profiles drop quickly. This indicates that the larger bubbles in a given flow rate tend to remain in the central region of the channel, whereas the smaller bubbles remain close to the wall. The difference in values between the regions may occur due to the optical distortion between the camera and the channel when the camera is moved vertically to the test section.

Other than the velocity, void fraction, and size the shadowgraphy method was able to provide the velocity fluctuations and Reynolds stresses. The full channel region was considered for both parameters (in shadowgraphy and PTV). The RMS, shown with each component plotted separately in Figs. 44-49, signifies the fluctuations in the instantaneous velocity from the average velocity. In other words, large RMS values would occur from large fluctuations in the flow due to the constantly changing instantaneous velocity. The high and medium flow rates seem to have a fairly constant fluctuating velocity in the center of the channel, whereas the low flow rate shows a constantly changing fluctuation throughout the channel. Also note how the RMS values of u and v change as the flow rate is decreased: u decreases and v increases. This means that the fluctuations of the radial component of the velocity decreases and those of the axial component increase. It suggests that larger bubbles oscillate more frequently than smaller bubbles. All plots, except Fig. 48, show that the RMS for both sections is fairly similar.

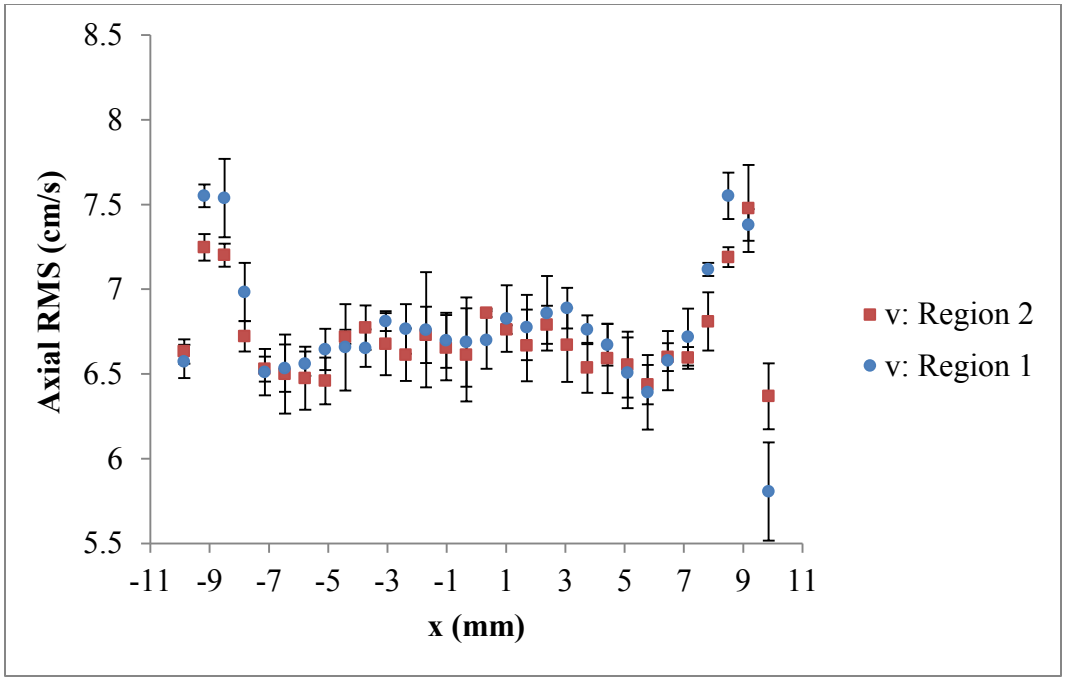

Figure 44: Average axial RMS for bubble velocity in both regions for j_g = 4.6 mm/s.

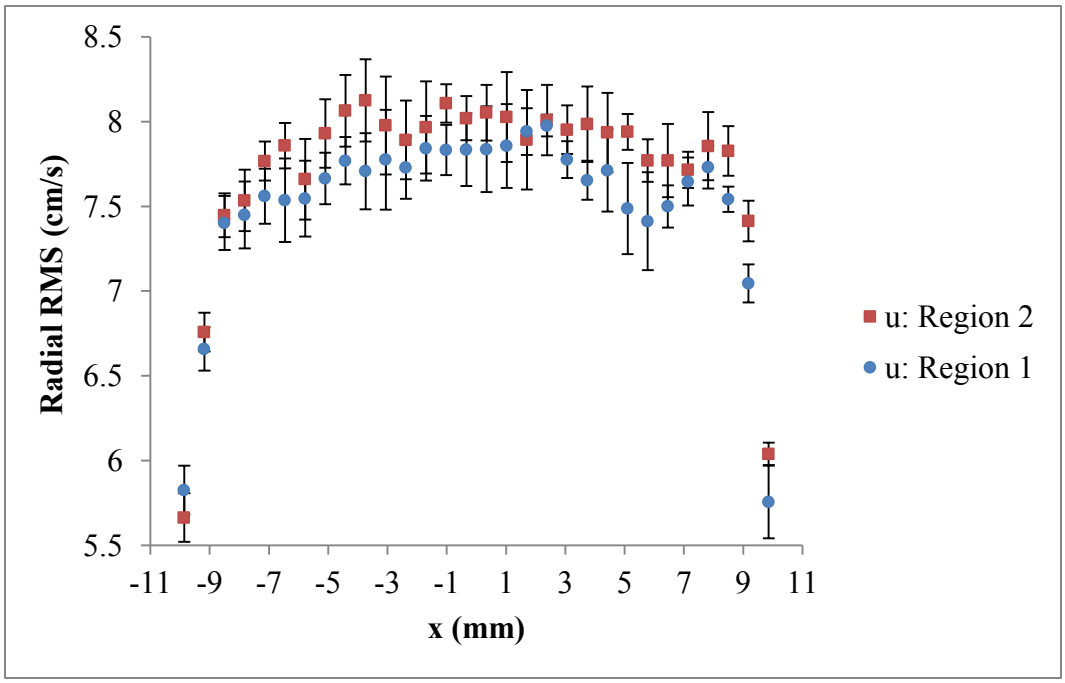

Figure 45: Average radial RMS for bubble velocity in both regions for j_g = 4.6 mm/s.

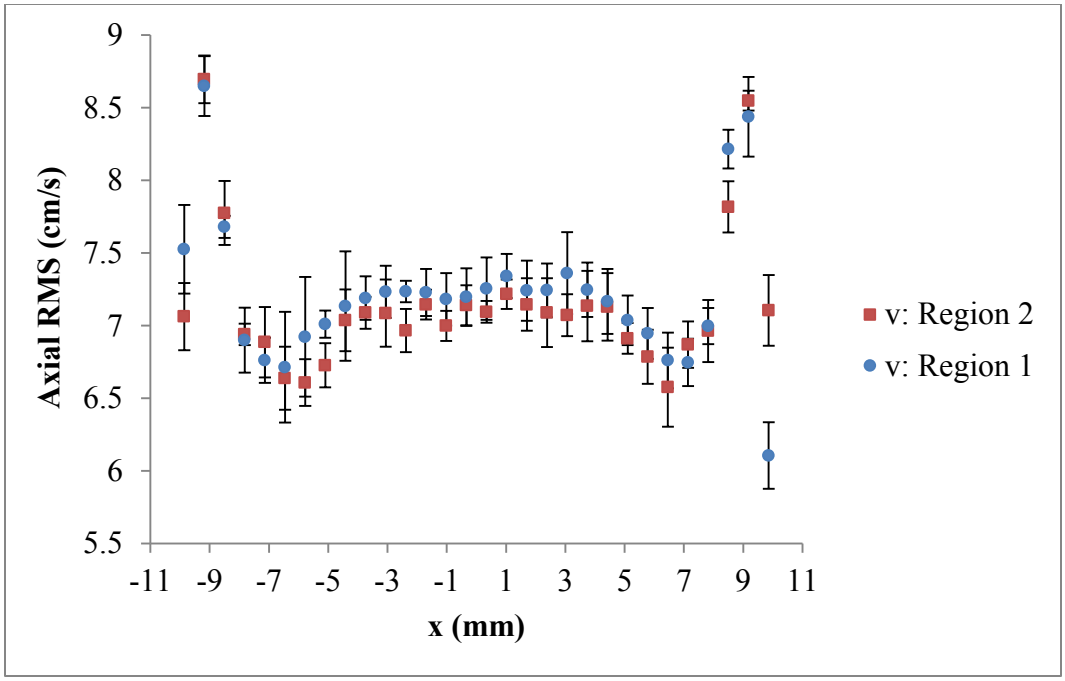

Figure 46: Average axial RMS for bubble velocity in both regions for j_g = 2.5 mm/s.

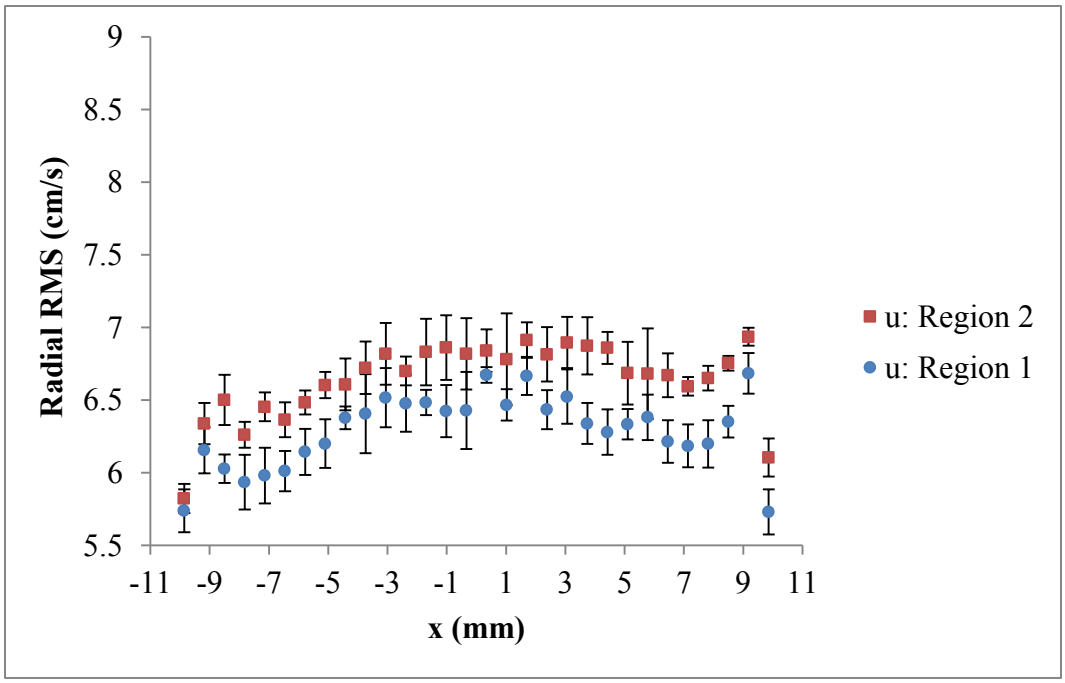

Figure 47: Average radial RMS for bubble velocity in both regions for j_g = 2.5 mm/s.

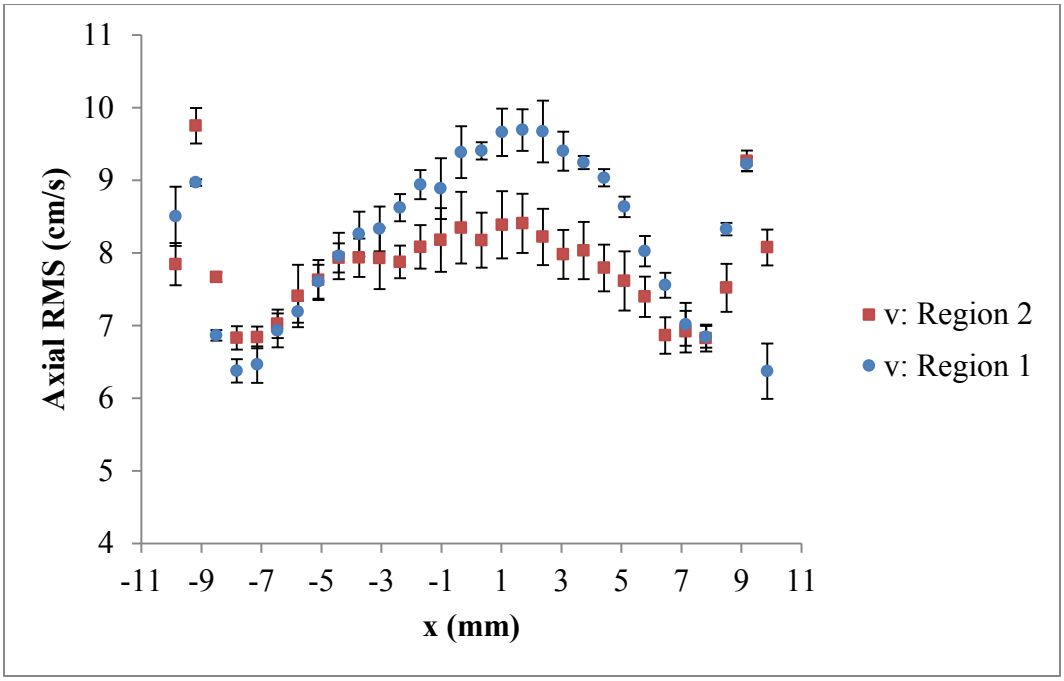

Figure 48: Average axial RMS for bubble velocity in both sections for j_g = 1.4 mm/s.

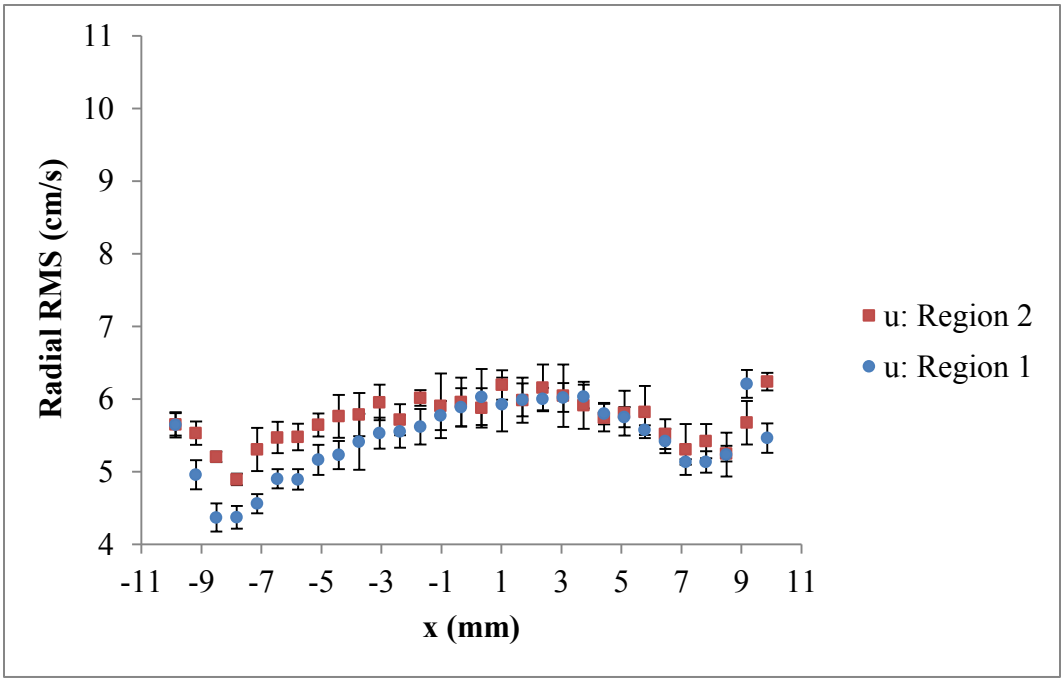

Figure 49: Average radial RMS for bubble velocity in both regions for j_g = 1.4 mm/s.

The Reynolds stresses obtained from shadowgraphy are shown in Figs. 50-52. All three figures show large changes near the walls. This may be due to the large velocity gradient occurring in that area (see the large difference in the centroid velocity from x=7-11 mm in Figs. 35-37). Note the increase in the peak values as the flow rate decreases. The Reynolds stresses show that as the flow rate decreases the bubble centroid velocity increases and causes a larger velocity gradient close to the wall. An interesting observation from Fig. 52 is the comparatively flat profile in the center of the channel. Even though the velocity distribution (Fig. 37) shows change in the center of the channel, there seems to be no indication of that in the Reynolds stresses. It may be due to the low magnitude of the gradient near the center compared to the high gradient near the wall. A similar profile for the Reynolds stresses was found for both sections.

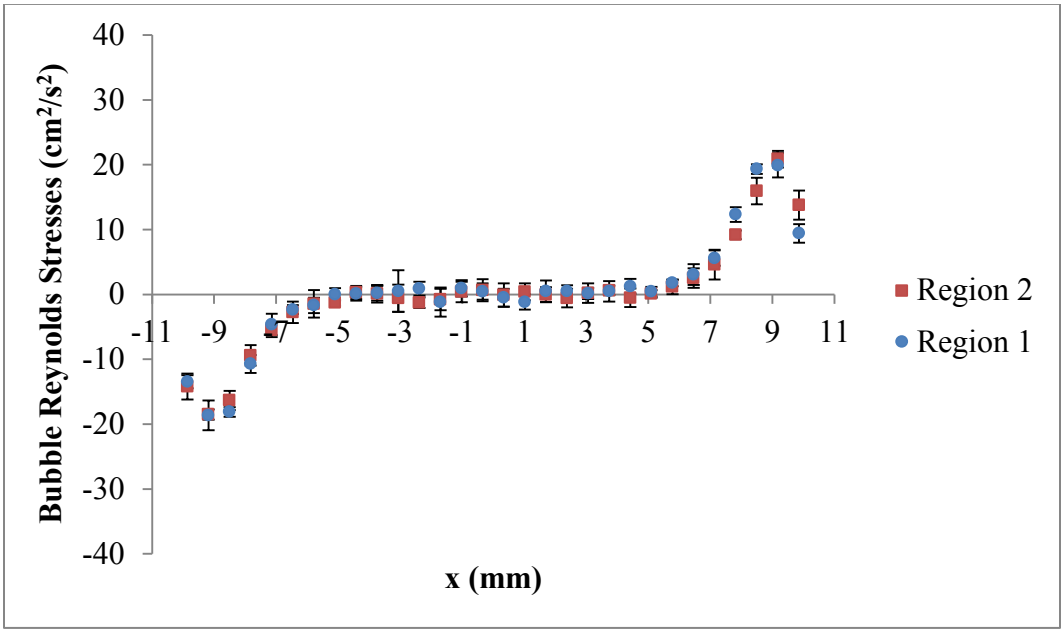

Figure 50: Average bubble Reynolds stresses in both regions for j_g = 4.6 mm/s.

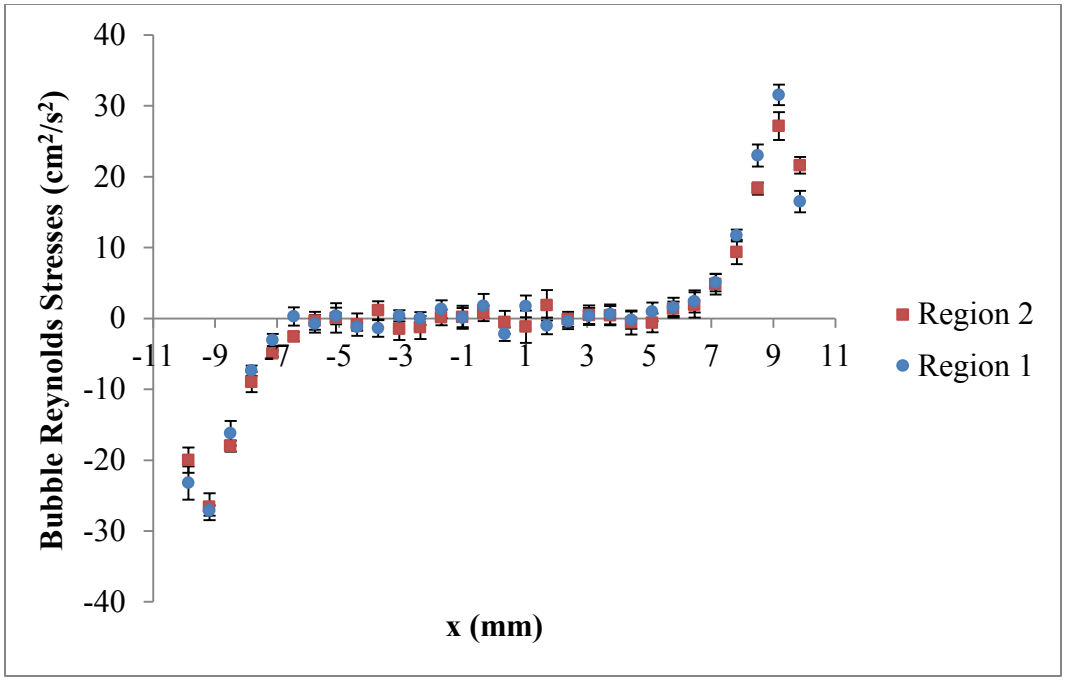

Figure 51: Average bubble Reynolds stresses in both regions for j_g = 2.5 mm/s.

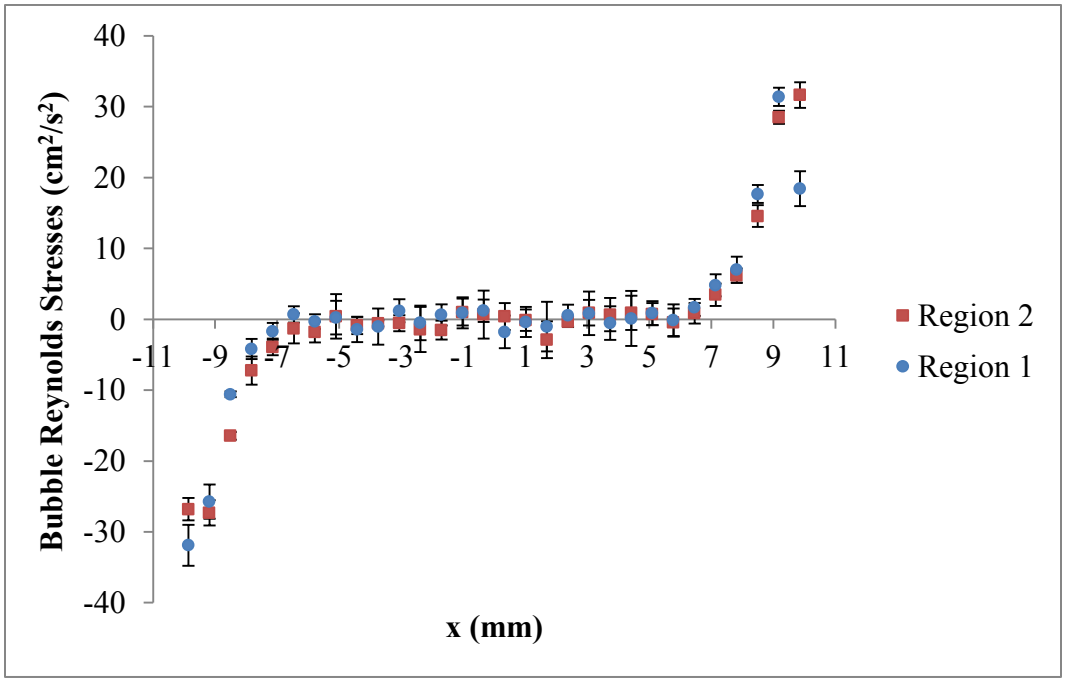

Figure 52: Average bubble Reynolds stresses in both regions for j_g = 1.4 mm/s.

4.2.3 PTV results

The liquid velocity, fluctuations in the velocity, and Reynolds stresses were parameters provided by the tracking algorithm for the liquid phase. Although there was no liquid flow in the channel, the bubble motion caused movement of the surrounding liquid. Figures 53-55 show the average liquid velocity distribution of the axial and radial components for the three flow rates. Movement of the radial component of the velocity can be considered negligible compared to the axial component. The axial component of the velocity displays a profile but seems to have no defined pattern as the flow rate decreases. In Fig. 53, a decrease and increase in v is observed as the profile approaches the wall. The recirculation of the liquid, which was visually confirmed near the wall, is causing the large change. Notice the positive value in the center of the channel indicates that the liquid is moving along the direction of the bubbles. On the contrary, the medium flow rate shows that the bulk liquid is slightly moving in the opposite direction of bubble motion (for Region 1). Going from the high flow rate to medium, the number of bubbles increased but the size decreased. The negative velocity may be due to the presence of smaller and abundant bubbles in the channel. The bubble velocity profile may also have an effect on the liquid velocity. Figure 36 shows a flat bubble velocity profile followed by a decrease near the wall. The opposite is shown by Fig. 54 in which the majority of the liquid has been displaced and is flowing downwards (Region 1) except near the wall where the bubble velocity drops and the liquid velocity rises. The velocity for Region 2 is approximately zero. The profile for the low flow rate seems to be completely opposite from the other two flow rates. The majority of the liquid is flowing upwards and near the

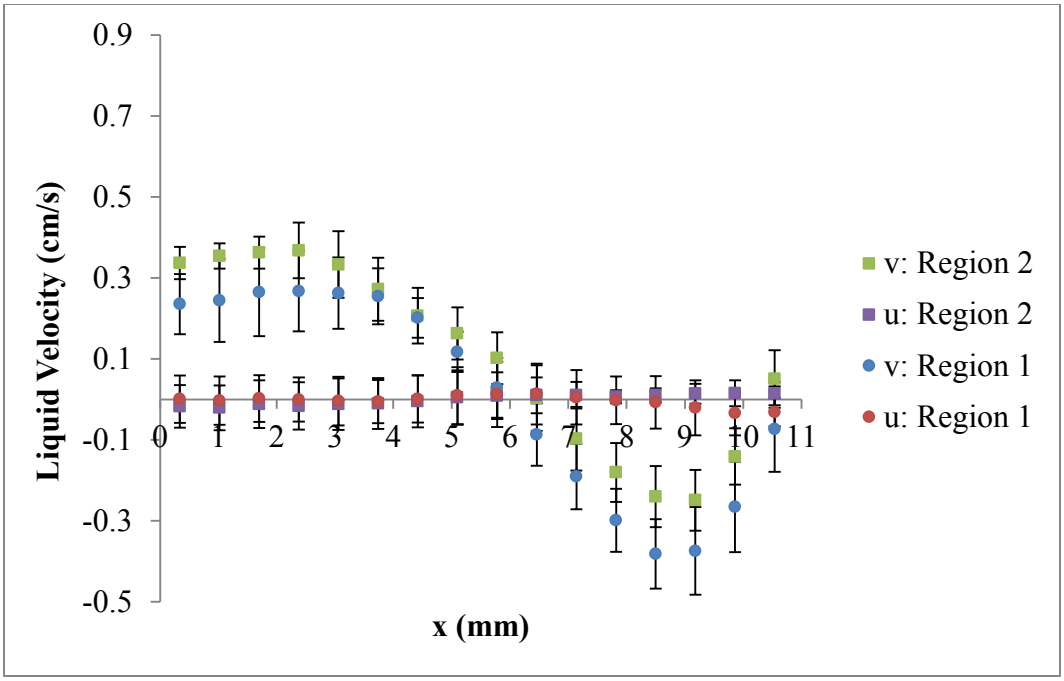

Figure 53: Average liquid velocity in both regions for j_g = 4.6 mm/s.

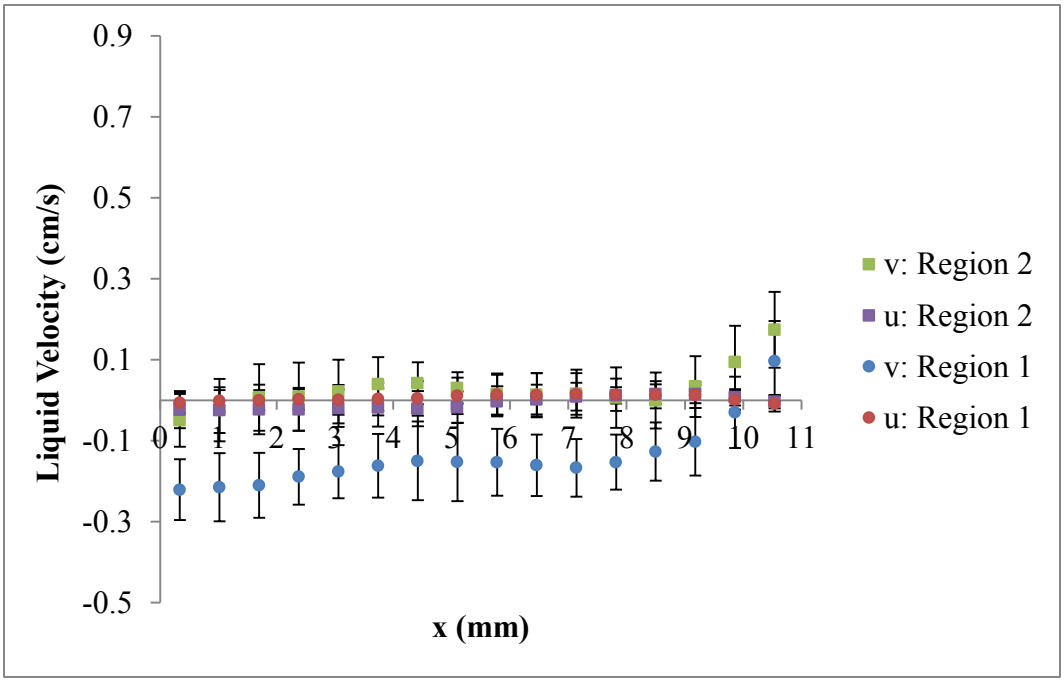

Figure 54: Average liquid velocity in both regions for j_g = 2.5 mm/s.

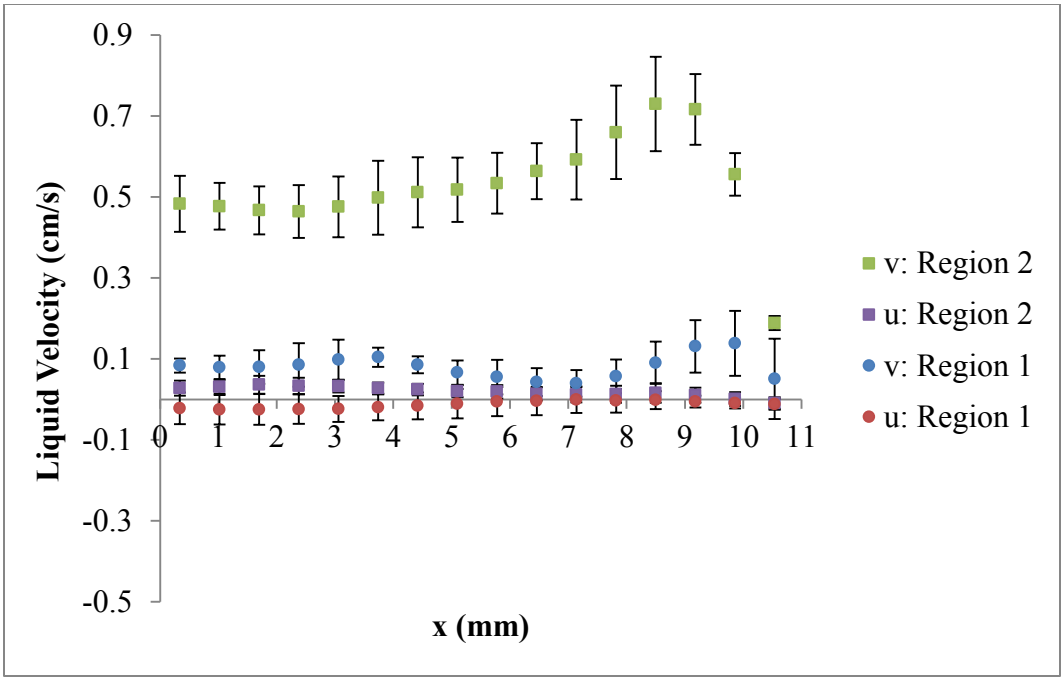

Figure 55: Average liquid velocity in both regions for j_g = 1.4 mm/s.

wall it flows downwards for both regions. Region 1 axial velocity can be considered negligible compared to Region 2 velocity. The size of the bubbles was the smallest in the low flow rate and the quantity was also lower than the other flow rates. The change in the profile may be attributed to the local effects of the small bubbles, since not many larger sized bubbles were present. Even though a transition may exist between the flow rates, it is not evident with three flow rates. Additional flow rates are necessary to confirm the transition between the current flow rates.

More measurement time may be required for the medium and low flow rates due to the small liquid displacement in these flow rates. The bubbles in the large flow rate displace more liquid and 10,918 images may be sufficient to calculate the average

profile. In the case of the other two flow rates, the same amount of images may not be sufficient. The resulting profiles may only capture the local effects of the liquid motion near the bubble. To obtain a more accurate average of the region, more images are required.

The difference between the liquid velocity profiles for both sections increased as the flow rate decreased. The axial component of the velocity is very similar for both sections in Fig. 53, with slightly higher magnitude for Region 2. Figure 54 shows a higher axial velocity for Region 2. This may be due to the bubble velocity, since any change in the bubble motion directly affects the liquid. Figure 55 shows a vast difference of the axial velocity between the two regions. Fig. 37 provides an explanation as to why the liquid velocity would be higher for Region 2: higher bubble velocity. The bubbles travel faster in the second region. As a result they would have a larger effect on the liquid, since smaller bubbles cause more local effects. Notice the general shape of the profiles for each flow rate in both regions. The magnitude of the value changes, but the distribution exhibits a similar shape. Although the liquid motion was found to be random, the figures show an average trend exists in the channel for each flow rate. Observe that the liquid velocity is negligible when compared to the bubble velocity.

The change in the RMS measured from PTV (Figs. 56-58) was less than the value measured from shadowgraphy. Since bubble velocity is greater than the liquid velocity, the liquid fluctuations would result in a smaller magnitude. Notice the decrease in the values of the fluctuations as the flow rate decreases. Due to the large liquid disturbance caused by the large bubbles, the fluctuation value is highest for j_g = 4.6

mm/s. On the other hand, smaller bubbles will cause smaller liquid disturbance. Therefore the low flow rate has the lowest fluctuation values. The RMS had similar profiles for both sections except close to the walls. The progression of the fluctuations close to the wall for Region 2 can be seen as the flow rate decreases. In Fig. 56 the RMS is quite similar for both regions. Figure 57 shows a slightly increased profile near the wall and it increases even further in Fig. 58. From the figures it is observed that as the flow rate decreases the liquid fluctuations increase close to the wall. This occurs from the large variation in the instantaneous bubble velocity (peaks in Figs. 44-49) near the wall as the flow rate is reduced.

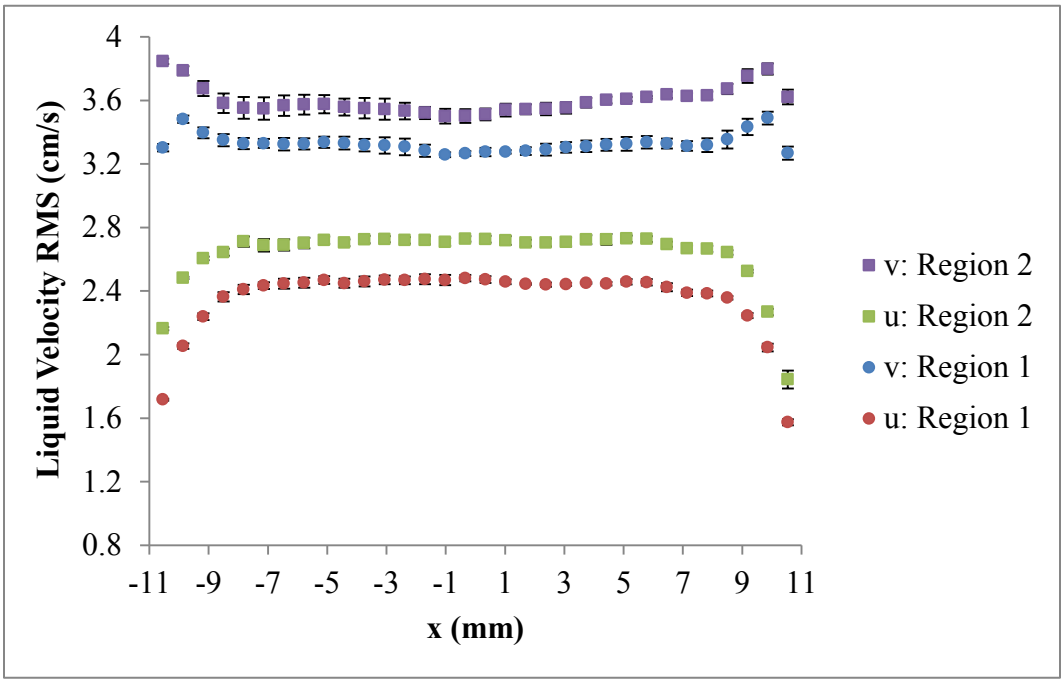

Figure 56: Average liquid RMS in both regions for j_g = 4.6 mm/s.

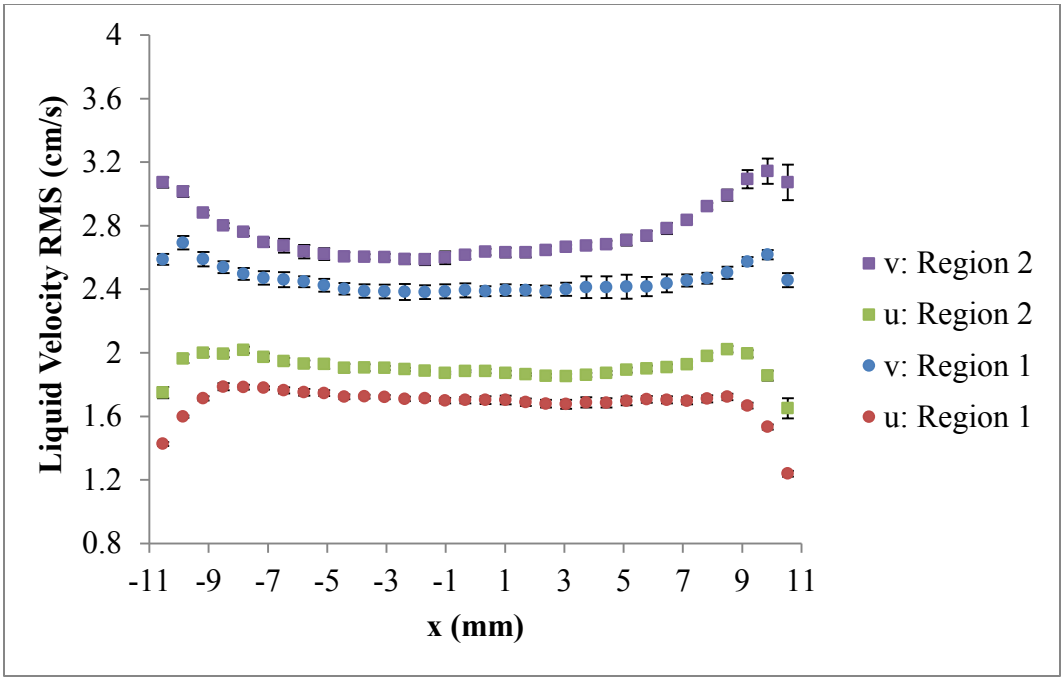

Figure 57: Average liquid RMS in both regions for j_g = 2.5 mm/s.

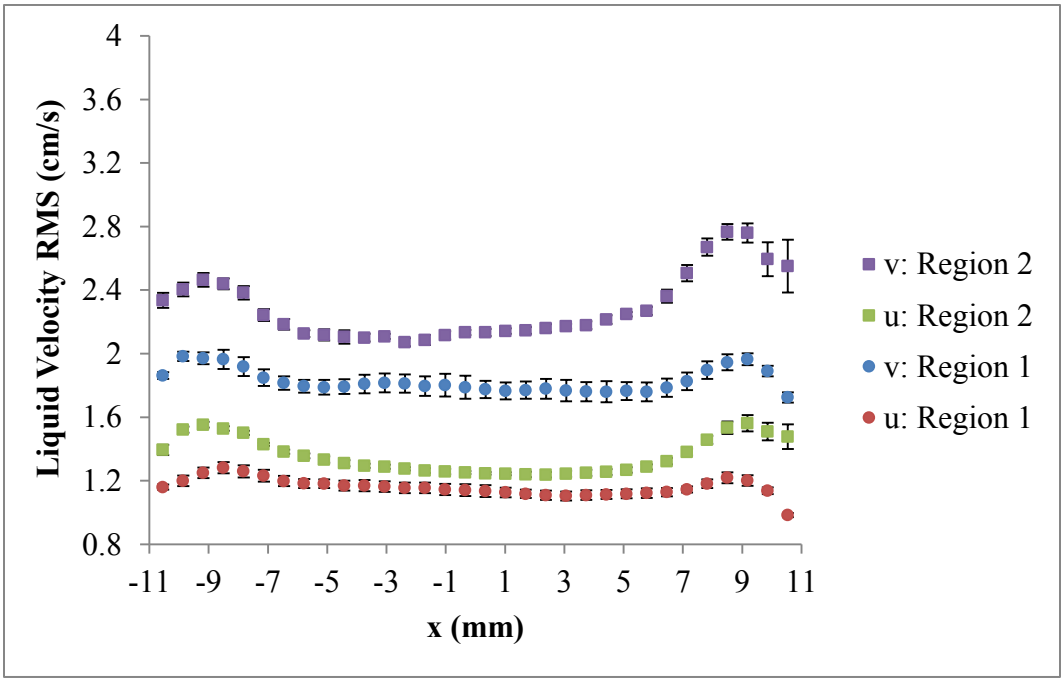

Figure 58: Average liquid RMS in both regions for j_g = 1.4 mm/s.

The Reynolds stresses obtained from PTV are shown in Figs. 59-61. Unlike those from shadowgraphy, the Reynolds stresses show a changing profile throughout the channel. The gradient of the velocity profiles do not change dramatically near the center in Figs. 54 and 55, indicating that the Reynolds stresses would show a similar trend as displayed in Figs. 60 and 61. The change in velocity gradient is more significant near the wall than in the center. As a result, the Reynolds stresses are fairly constant in that region of the channel. The Reynolds stresses have similar trends for both sections, except for the low flow rate case which shows a slightly different profile near the center of the channel.

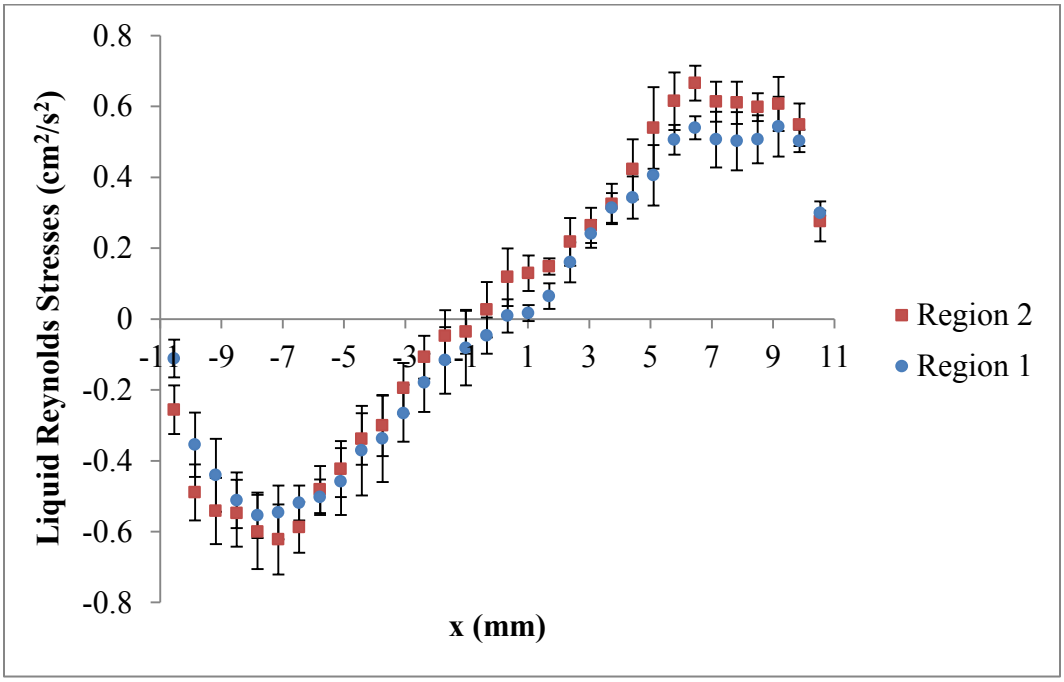

Figure 59: Average liquid Reynolds stresses in both regions for j_g = 4.6 mm/s.

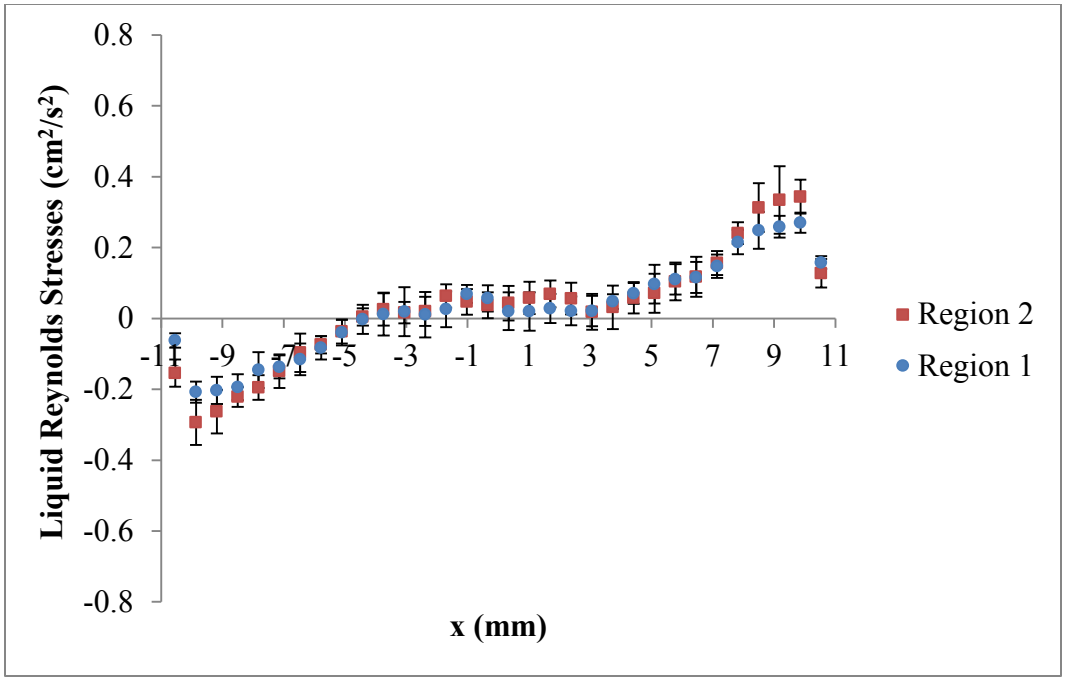

Figure 60: Average liquid Reynolds stresses in both regions for j_g = 2.5 mm/s.

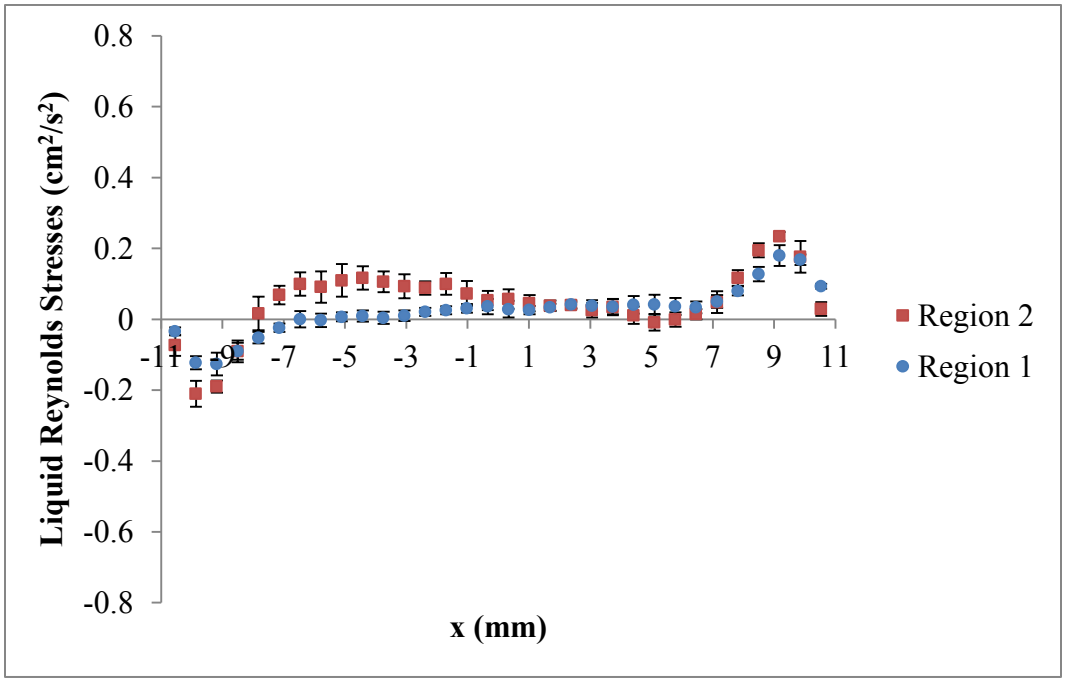

Figure 61: Average liquid Reynolds stresses in both regions for j_g = 1.4 mm/s.

CHAPTER V

CONCLUSION AND FUTURE WORK

5.1 Conclusion

Two techniques, an optical probe and a tracking algorithm, were successfully applied in this experiment to obtain two-phase flow parameters in a square channel. The study was performed in two regions far from the bubble injection location. Air was inserted into the channel at three superficial gas velocities: 4.6 mm/s, 2.5 mm/s, and 1.4 mm/s. Using an in-house developed tracking algorithm, 2-D measurements were taken with PTV and shadowgraphy. PTV provided liquid parameters such as the velocity, fluctuations in the velocity, and Reynolds stresses. Shadowgraphy was able to provide bubble parameters such as the centroid velocity, fluctuations in the velocity, void fraction, size, and Reynolds stresses. Additionally, an optical probe was placed in the channel to measure the bubble interface velocity, void fraction, bubble frequency, time of flight, and Sauter mean diameter.

From the previous study performed, it was shown that a new bubble sample after each image pair (every two images) had an enormous effect on the velocity profiles. The explanation was given as to why a difference exists between the same parameters obtained from the optical probe and shadowgraphy. Mainly, the measurement technique of each method caused the difference in the results. Due to the point measurement nature of the optical probe all calculations were based on the line of impact through the bubble, whether it was at the center or the edge of the bubble. Also, the probe-bubble interaction

produced more surface deformations and affected the interface velocity. A dimensional disagreement was involved in shadowgraphy results. The 3-D volume was projected to a 2-D plane, which caused the void fraction results to be much greater than those obtained from the optical probe.

Most parameters were found to be in good agreement for both regions and all three methods. The only profiles from the optical probe results that displayed a difference between the two regions were the void fraction and interface velocity (resulting from the time of flight). It was believed that the difference in the void fraction was caused by a change in the bubble frequency, since a variation was observed. As for the interface velocity, slower moving bubbles and the activation of different pores in the porous media were believed to have caused the difference between the two regions. In the shadowgraphy results the bubble centroid velocity for the low flow did not show similar profiles for both regions. It is believed the bubbles were traveling faster in the second region since the low flow rate was not fully developed. The PTV results for the liquid phase showed changes between the two regions. The difference in the axial velocity profiles between the two regions was found to increase as the flow rate was reduced.

After concluding the experiment it was realized that the optical probe underestimates the gas phase parameters and shadowgraphy overestimates them due to their measurement method. The only exception in the estimation was the bubbly velocity. PTV was the most precise in its measurement method since only particles present in the laser light plane were tracked, although in some parts of the images the

liquid is covered by bubbles. It is believed the data obtained from this experiment will assist in improving and validating current simulations.

5.2 Considerations for future work

Enhancements can be made and other methods/techniques can be applied in this experiment to improve the two-phase flow study. As mentioned earlier, additional flow rates applied to the same experiment may show the transition between the current flow rates. Also, more measurement time is required for the lower flow rates in order to confirm if any changes will occur in the present profiles from analyzing more images. A simple addition to the experiment would be to place an HFA in the channel. It would provide point measurements of the liquid phase, just as the optical probe provided point measurements of the gas phase. The Stereoscopic/3-D method can be applied to increase the amount of information obtained since an issue with shadowgraphy was the dimensional disagreement. It would also provide more information for the liquid phase (PTV). Even though it is considered a point measurement technique, LDV may prove to be a verification method for parameters obtained from the other techniques.

REFERENCES

Canaan, R., Hassan, Y., Blanchat, T., Seeley Jr, C., 1992. Simultaneous velocity measurements of both components of a two-phase flow using particle image velocimetry. International Journal of Multiphase Flow 18, 371–395.

Chaumat, H., Billet-Duquenne, A., Augier, F., Mathieu, C., Delmas, H., 2005. Application of the double optic probe technique to distorted tumbling bubbles in aqueous or organic liquid. Chemical Engineering Science 60, 6134–6145.

Chaumat, H., Billet-Duquenne, A., Augier, F., Mathieu, C., Delmas, H., 2007. On the reliability of an optical fibre probe in bubble column under industrial relevant operating conditions. Experimental Thermal and Fluid Science 31, 495–504.

Dahikar, S., Sathe, M., Joshi, J., 2010. Investigation of flow and temperature patterns in direct contact condensation using PIV, PLIF and CFD. Chemical Engineering Science 65, 4606–4620.

Estrada-Perez, C., 2004. Analysis, comparison and modification of various Particle Image Velocimetry (PIV) algorithms. M.S. thesis, Texas A&M University.

Estrada-Perez, C., Hassan, Y., 2010. PTV experiments of subcooled boiling flow through a vertical rectangular channel. International Journal of Multiphase Flow 36, 691–706.

Johansen, J., 2010. Full-scale two-phase flow measurements using optical probes on Athena II research vessel. M.S. thesis, University of Iowa, Iowa City.

Kataoka, I., Ishii, M., Serizawa, A., 1986. Local formulation and measurements of interfacial area concentration in two-phase flow. International Journal of Multiphase Flow 12, 505–529.

Khan, A., Estrada-Perez, C., Hassan, Y., 2011. Whole-field velocity measurements of isothermal bubble plume using PTV. Proceedings from 19th International Conference on Nuclear Engineering, JSME ICONE19-44083.

Kiambi, S., Duquenne, A., Dupont, J., Colin, C., Risso, F., Delmas, H., 2003. Measurements of bubble characteristics: comparison between double optical probe and imaging. The Canadian Journal of Chemical Engineering 81, 764–770.

Končar, B., Kljenak, I., Mavko, B., 2004. Modeling of local two-phase flow parameters in upward subcooled flow boiling at low pressure. International Journal of Heat and Mass Transfer 47, 1499–1513.

Lima Neto, I., Zhu, D., Rajaratnam, N., 2008. Bubbly jets in stagnant water. International Journal of Multiphase Flow 34, 1130–1141.

Lindken, R., Merzkirch, W., 2002. A novel PIV technique for measurements in multiphase flows and its application to two-phase bubbly flows. Experiments in Fluids 33, 814–825.

Mudde, R. F., Harteveld, W. K., van den Akker, H. E. A, 2008. Uniform Flow in Bubble Columns. Industrial & Engineering Chemistry Research 48, 148–158.

Ramstorfer, F., Steiner, H., Brenn, G., 2008. Modeling of the microconvective contribution to wall heat transfer in subcooled boiling flow. International Journal of Heat and Mass Transfer 51, 4069–4082.

Rensen, J., Roig, V., 2001. Experimental study of the unsteady structure of a confined bubble plume. International Journal of Multiphase Flow 27, 1431–1449.

Revankar, S., Ishii, M., 1992. Local interfacial area measurement in bubbly flow. International Journal of Heat and Mass Transfer 35, 913–925.

Roy, R., Kang, S., Zarate, J., Laporta, A., 2002. Turbulent subcooled boiling flow—experiments and simulations. Journal of Heat Transfer 124, 73.

Sathe, M., Thaker, I., Strand, T., Joshi, J., 2010. Advanced PIV/LIF and shadowgraphy system to visualize flow structure in two-phase bubbly flows. Chemical Engineering Science 65, 2431–2442.

Vejražka, J., Večeř, M., Orvalho, S., Sechet, P., Ruzicka, M., Cartellier, A., 2010. Measurement accuracy of a mono-fiber optical probe in a bubbly flow. International Journal of Multiphase Flow 36, 533–548.

Yeoh, G., Tu, J., Lee, T., Park, G., 2002. Prediction and measurement of local two-phase flow parameters in a boiling flow channel. Numerical Heat Transfer, Part A 42, 173–192.

Zaruba, A., Krepper, E., Prasser, H., Reddy Vanga, B., 2005. Experimental study on bubble motion in a rectangular bubble column using high-speed video observations. Flow Measurement and Instrumentation 16, 277–287.

VITA

Abdul R. Khan received his Bachelor of Science degree in Applied Physics from New Jersey Institute of Technology in 2009. He entered the Nuclear Engineering program at Texas A&M University in January 2010 and received his Master of Science degree in August 2012.

Mr. Khan may be reached at 15123 Rockdale Bridge Lane, Sugarland, TX 77498. His email is ark8@njit.edu.